Astronomy & Astrophysics

Searching for intergalactic star forming regions in Stephan's Quintet with SITELLE

I. Ionised gas structures and kinematics⋆

S. Duarte Puertas[1], J. Iglesias-Páramo[1,2], J. M. Vilchez[1], L. Drissen[3,4], C. Kehrig[1], and T. Martin[3,4]

[1] Instituto de Astrofísica de Andalucía – CSIC, Glorieta de la Astronomía s.n., 18008 Granada, Spain
e-mail: salvini@iaa.es
[2] Estación Experimental de Zonas Áridas – CSIC, Ctra. de Sacramento s.n., La Cañada, Almería, Spain
[3] Département de Physique, de Génie Physique et d'Optique, Université Laval, Québec, QC G1V 0A6, Canada
[4] Centre de Recherche en Astrophysique du Québec, Québec, Canada

ABSTRACT

Stephan's Quintet (SQ), the prototypical compact group of galaxies in the local Universe, has been observed with the imaging Fourier transform spectrometer SITELLE, attached to the Canada-France-Hawaii-Telescope, to perform a deep search for intergalactic star-forming emission. In this paper we present the extended ionised gaseous structures detected and analyse their kinematical properties. The large field of view ($11' \times 11'$) and the spectral ranges of SITELLE have allowed a thorough study of the entire galaxy system, its interaction history and the main properties of the ionised gas. The observations have revealed complex three-dimensional strands in SQ seen for the first time, as well as the spatially resolved velocity field for a new SQ dwarf galaxy (M 82-like) and the detailed spectral map of NGC 7320c, confirming its AGN nature. A total of 175 SQ Hα emission regions have been found, 22 of which present line profiles with at least two kinematical components. We studied 12 zones and 28 sub-zones in the SQ system in order to define plausible physical spatial connections between its different parts in the light of the kinematical information gathered. In this respect we have found five velocity systems in SQ: (i) $v = [5600-5900]$ km s^{-1} associated with the new intruder and the southern debris region; (ii) $v = [5900-6100]$ km s^{-1}, associated with the north starburst A and south starburst A and the strands connected to these zones; (iii) $v = [6100-6600]$ km s^{-1}, associated with the strands from the large-scale shock region (LSSR); (iv) $v = [6600-6800]$ km s^{-1}, associated with the young tidal tail, the starburst A (SQA), NGC 7319, and the NGC 7319 north lobe; and (v) $v = [6800-7000]$ km s^{-1}, associated with the strands seen connecting LSSR with SQA. We fail to detect ionised gas emission in the old tail, neither in the vicinity of NGC 7318A nor in NGC 7317, and the connection between NGC 7319 north lobe and SQA cannot be confirmed. Conversely, a clear gaseous bridge has been confirmed both spatially and kinematically between the LSSR zone and the NGC 7319 AGN nucleus. Finally, a larger scale, outer rim winding the NGC 7318B/A system clockwise north-west to south-east has been highlighted in continuum and in Hα. This structure may be reminiscent of a sequence of a previously proposed scenario for SQ a sequence of individual interactions.

Key words. galaxies: evolution – galaxies: groups: general – galaxies: kinematics and dynamics – galaxies: star formation

1. Introduction

Stephan's Quintet (SQ, Stephan 1877) is one of the most studied galaxy aggregates and it represents a unique laboratory for understanding how a compact group evolves. SQ is composed of elliptical (NGC 7317 and NGC 7318A) and spiral galaxies (NGC 7319, NGC 7320c, and NGC 7318B). NGC 7318B is a gas-rich galaxy that has experienced several interactions throughout its evolution (e.g. Moles et al. 1997; Sulentic et al. 2001). One foreground spiral galaxy (NGC 7320) with a discordant redshift (Burbidge & Burbidge 1961) can also be seen in the field of view (FoV) of SQ.

Moles et al. (1997) and Sulentic et al. (2001) suggested that compact groups of galaxies are formed by acquiring intruder galaxies associated with a large-scale structure. All the galaxies of SQ, except NGC 7318B, have evolved dynamically, los-

ing their interstellar medium (ISM). Moles et al. (1997) proposed an evolutionary model for SQ based on two intruders, an old intruder (OI, NGC 7320c) and a new intruder (NI, NGC 7318B). SQ is at an advanced state of interaction, evidenced by the existence of, for example, at least young and old tidal tails with ages of $150-200$ Myr and $400-500$ Myr, respectively (Fedotov et al. 2011); a large-scale shock region (LSSR, e.g. Allen & Hartsuiker 1972; Ohyama et al. 1998; Iglesias-Páramo et al. 2012) produced by an ongoing interaction between NGC 7318B and both NGC 7319 and debris material from previous interactions; a diffuse gas halo close to NGC 7317 composed by old stars that indicates that the formation of SQ took place several Gyr ago (Duc et al. 2018).

From the kinematical point of view, SQ covers a large radial velocity range ($\sim$5500 to $\sim$6600 km s^{-1}). The core of SQ (i.e. NGC 7317, NGC 7318A, and NGC 7319) and NGC 7320c show a mild radial velocity dispersion, whereas NGC 7318B has an unusually high radial velocity dispersion compared to the others ($\Delta V \sim 1000$ km s^{-1}), indicating that it is not bound to the SQ (Trinchieri et al. 2005). Classically, two radial velocity structures

were detected by Sulentic et al. (2001): the gas associated with the SQ and the gas associated with NI, where most of the emission detected in the ISM comes from the NI. Iglesias-Páramo et al. (2012) observed three radial velocity components but could only focus on the lower part of the shock. The LSSR spans a wide range of redshift (e.g. Konstantopoulos et al. 2014). Its structure and gas distribution have not been entirely examined until now due to the inability to fully study the system (from NGC 7320c to NGC 7317).

SQ has been widely researched with different wavelengths by many authors: with radio (e.g. Williams et al. 2002; Lisenfeld et al. 2004; Guillard et al. 2012); ultraviolet (e.g. Xu et al. 2005; de Mello et al. 2012); X-ray (e.g. Trinchieri et al. 2003; Heida et al. 2012); infrared (e.g. Appleton et al. 2006, 2017; Cluver et al. 2010; Guillard et al. 2009); and visible (e.g. Moles et al. 1998; Iglesias-Páramo & Vílchez 2001; Sulentic et al. 2001; Mendes de Oliveira et al. 2004; Iglesias-Páramo et al. 2012; Trancho et al. 2012; Konstantopoulos et al. 2014; Rodríguez-Baras et al. 2014). There are also photometric studies (e.g. Gallagher et al. 2001; Fedotov et al. 2011; Duc et al. 2018) and simulations (e.g. Renaud et al. 2010; Hwang et al. 2012). Finally, several previous interferometric Fabry-Perot studies of the SQ (e.g. Sulentic et al. 2001; Mendes de Oliveira et al. 2001) have been done with diverse spatial coverages in wavelength-velocity resolution, though sometimes making difficult the discrimination between the emission of nearby lines at different velocities.

This work is based on the spectroscopic data from SITELLE (Grandmont et al. 2012), an imaging Fourier transform spectrometer (IFTS), attached to the Canada-France-Hawaii Telescope (CFHT). SITELLE allows us to study, for the first time, a large FoV considering the optical spectrum ranging from the UV atmosphere limit to the red, in order to study the physical, chemical, and kinematical properties of the entire SQ area. Our study presents an extensive spectral mapping that covers from the inner SQ "core" to the large gas halo surrounding the SQ. SITELLE observations offer us a great opportunity to perform an unbiased search for the star forming and tidal emission regions (e.g. tidal dwarf galaxies, TDG) present in the SQ in order to study their origin and properties. These data also provide a detailed spectroscopic mapping of the extended shock zone and its associated emission, with a seeing limited spatial resolution (~0.8″). This is relevant to obtain a more complete view of the ionisation structure of the shock and its environment, discriminating in velocity space the shock ionised gas from other intervening gaseous material (e.g. HII regions from the arms of the central spiral galaxies, gas associated with the AGN main galaxy).

The structure of this paper is organised as follows: in Sect. 2 we describe the data and the methodology used to select the Hα emission regions from the SQ. We detail our main results in Sect. 3. Finally, the discussion and main conclusions of our work are presented in Sect. 4. Line fluxes within the SN1, SN2, and SN3 data cubes, and the study of the physical properties and excitation conditions of the gas, will be presented in a future paper (Duarte Puertas et al., in prep., Paper II). Throughout the paper, we assume a Friedman-Robertson-Walker cosmology with $\Omega_{\Lambda 0} = 0.7$, $\Omega_{m0} = 0.3$, and $H_0 = 70$ km s^{-1} Mpc^{-1}.

2. Observations and data analysis

2.1. Observations

SITELLE is an IFTS that aims to study the spatially-resolved spectra of extended sources. It has a FoV of $11' \times 11'$ (0.32″ per pixel, Drissen et al. 2019), suitable for investigating complex

Table 1. Observing parameters.

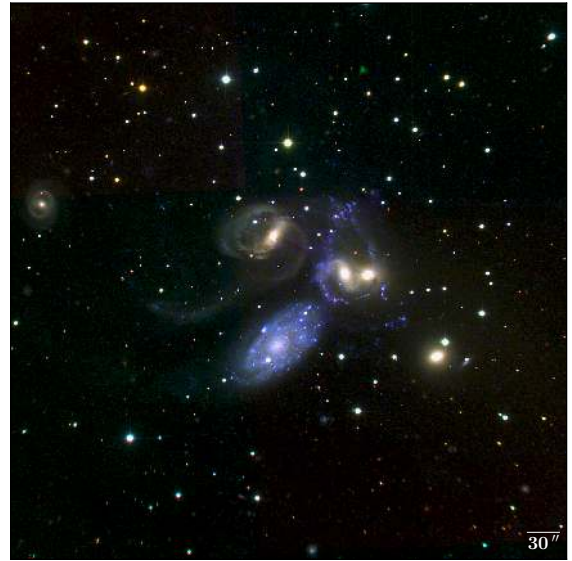| (1) Filter	(2) SN1	(3) SN2	(4) SN3
RA (h m s)	22:36:05.30	22:36:05.30	22:36:05.84
Dec (° ′ ″)	33:58:59.9	33:58:59.9	33:59:09.6
Observing date	2016-07-09	2016-07-10	2015-08-07
			2015-08-08
Spectral range $T > 90\%$ (nm)	363−386	482−513	648−685
Number of steps	85	169	342
Exp. time/step (s)	75	65	25
Total exp. time (h)	1.77	3.05	2.37
Mean resolution, R	500	760	1560

Stephan's Quintet

Fig. 1. SITELLE deep-colour image of SQ composed using SN1, SN2, and SN3 data cubes. North is top and east is left. The distance considered for SQ in this paper is $d = 88.6$ Mpc (from the NASA/IPAC Extragalactic Database known as NED). At the distance of SQ, 30″ corresponds to ~13.04 kpc.

and extensive systems of galaxies such as SQ. The observations were carried out in August 2015 and July 2016 (P.I. Drissen) under an average seeing of ~0.8″. The three filters SN1, SN2, and SN3 were used to capture the emission lines of our interest: [O II]λ3727, [O III]$\lambda\lambda$4959,5007, Hβ, [N II]$\lambda\lambda$6548,6583, [S II]$\lambda\lambda$6716,6731, and Hα. Table 1 shows the observing parameters (right ascension or RA, declination or Dec, observing date, spectral range, number of steps, mean resolution, and the total exposure time) considered for each filter. Figure 1 shows a SITELLE deep-colour image of the SQ field composed using the integrated emission on the SN1, SN2, and SN3 data cubes (see Drissen et al. 2019, Sect. 5.4). We worked the data cubes in wavenumbers (cm^{-1}), which is SITELLE's natural units.

2.2. Reduction, calibration, and measurements

The data were fitted using the Python-based software ORCS (Martin et al. 2015). Data were recalibrated in wavelength using the OH sky lines that are visible in most parts of the FoV. We fitted the OH sky lines using the function SPECTRALCUBE.MAP_SKY_VELOCITY and the resulting corrections were implemented to

the cube using SPECTRALCUBE.CORRECT_WAVELENGTH (Martin et al. 2018). For each data cube, we subtracted the sky using the median sky spectrum from three dark regions (2700 pixels were used). For illustrative purposes, we show the median sky spectrum in the SN3 data cube in Fig. 2. In order to obtain a more precise radial velocity correction we used the function GET_RADIAL_VELOCITY_CORRECTION. Through this function, we found a shift of 15 km s^{-1} that was added to the measured velocity. The flux calibration was performed using the data cube of the standard star GD71. The Galactic extinction is very small, $E(B − V) = 0.07$, according to the NASA/IPAC Extragalactic Database known as NED[1], and we did not correct for it. The methodology used to analyse the data involved several steps that we describe below.

2.2.1. Searching for Hα emission

We considered a binning 3×3 to amplify the signal-to-noise ratio (∼450 000 pixels). In addition a study was done only in Hα for a binning 6×6 (see Sect. 3.3)[2] in order to unveil the lowest surface brightness gaseous emission in SQ. Subsequently, we searched for the wavenumber position (k_{max}) where the maximum intensity peak of the Hα emission line (A_{max}) is found in the typical wavenumber range of SQ ($\Delta K_{SQ} = [14820, 15021]$ cm^{-1}) and NGC 7320 ($\Delta K_{NGC 7320} = [15147, 15239]$ cm^{-1}), selecting the largest A_{max} between them. Once we found the position of the maximum intensity, we derived the standard deviation when the transmission curve is higher than 90% for the SN3 filter (std$_{90}$). To compute std$_{90}$, the typical wavenumber range for the emission lines Hα, [N II]$\lambda\lambda$6548,6583, and [S II]$\lambda\lambda$6716,6731 of each pixel have not been considered. We selected those pixels with $\frac{A_{max}}{std_{90}} \geq 2.5$ (∼25 800 pixels). We assumed that the maximum value corresponds to the Hα position. We know that the maximum in the AGN galaxy nucleus corresponds to [N II]λ6583 and this effect will be corrected later. We used the k_{max} value to derive the possible initial velocity for Hα (v_{ini}(Hα)) according to the following equation: $v_{ini}(Hα) = \left[\left(\left(\frac{1e7}{k_{max}\cdot\lambda(Hα)\cdot0.1}\right) - 1\right) \cdot c\right]$, where λ(Hα) = 6562.8 nm and $c = 299\,792$ km s^{-1}.

2.2.2. Identifying Hα emission regions

We fitted the spectrum for every selected pixel using the v_{ini}(Hα) derived above. Initially, we fitted each spectrum to a sincgauss function (the convolution of a Gaussian with a sinc function) for Hα and [N II]$\lambda\lambda$6548,6583 simultaneously. The theoretical relation [N II]λ6548/6583 = 0.333 is considered. When the broadening of the Hα line was lower than 70 km s^{-1}, we adjusted the spectrum using a sinc function (the instrumental line shape, Martin et al. 2016). When no emission was detected in [N II] λ6583, we refitted the spectrum only for the Hα emission line. The output parameters are the radial velocity, broadening, intensity peak, flux, and the corresponding uncertainties, as well as the standard deviation of each spectrum. After fitting the Hα line, we selected the pixels with contrast (Hα) = $\frac{A_{fit}}{std_{90}} \geq 5$, where A_{fit} is the intensity peak of the Hα emission line obtained from the fitting, and v_{ini}(Hα) ≥ 5000 km s^{-1} (∼950 pixels). Figure 3 shows the Hα flux (upper panel) and Hα radial velocity (lower panel) maps for the ∼2100 pixels (binning 3×3) with contrast
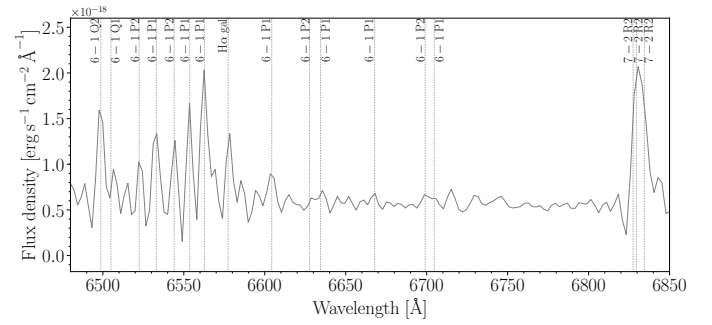

Fig. 2. Median sky spectrum in SN3 data cube (2700 pixels have been combined). The dashed vertical lines show multiple known OH sky lines.

(Hα) ≥ 5 and without velocity restrictions. We detect Hα emission in several galaxies: NGC 7319, NGC 7320c, NGC 7320 (the foreground galaxy with an average radial velocity of 786 km s^{-1}, see inset plot in the lower panel for more details), and the new dwarf galaxy in SQ (NG, see Sect. 3.4 and ID. 176 in Table B.1). Also, we detect Hα emission from the starbursts A and B (SQA and SQB, e.g. Xu et al. 1999). Additionally, this figure shows emission from the young tidal tail (YTT, e.g. Lisenfeld et al. 2002), LSSR, and the NI (e.g. Moles et al. 1997). We also detect emission to the left of NGC 7317; this region is discussed in depth in Sect. 3.4. From the sample of pixels selected above, we searched for all the Hα emission region candidates associated with the SQ. To do so, we first grouped the spatially associated emitting pixels. Then, the individual Hα regions associated with each group of pixels are defined searching for the local emission peaks in the Hα map using the Python-package ASTRODENDRO[3]; The membership of each group of pixels to a given individual Hα region has been defined from the segmentation method using the Python packages SCIPY.NDIMAGE and SKIMAGE.MORPHOLOGY.WATERSHED. This method allows us to define a population of 209 SQ Hα region candidates.

2.2.3. One velocity component analysis for each SQ Hα emission region

For each Hα emission region we obtained the integrated spectrum adding the flux of its pixels; then all integrated spectra were fitted using the ORCS function ORCS.FIT_LINES _IN_INTEGRATED_REGION. The spectral lines Hα and [N II] $\lambda\lambda$6548,6583 are fitted to a sincgauss function simultaneously, and when broadening of the Hα line is smaller than 70 km s^{-1}, a sinc function was used, as detailed above. As the beginning of the SN3 transmission curve coincides with the emission lines [S II]$\lambda\lambda$6716,6731 at SQ's redshift, we only take into account in the fit the spectral line [S II]λ6716 for those Hα emission regions with radial velocities lower than 6260 km s^{-1}, and [S II]λ6731 for those Hα emission regions with velocities lower than 5760 km s^{-1}. The output parameters are the radial velocity, broadening, intensity peak, total flux, and the corresponding uncertainties, as well as the standard deviation of each spectrum. The emission lines from the SN1 and SN2 data cubes were fitted using the velocity found in the previous step for Hα as a reference. It is important to note that we assumed the Hα radial velocity as the representative velocity for every Hα
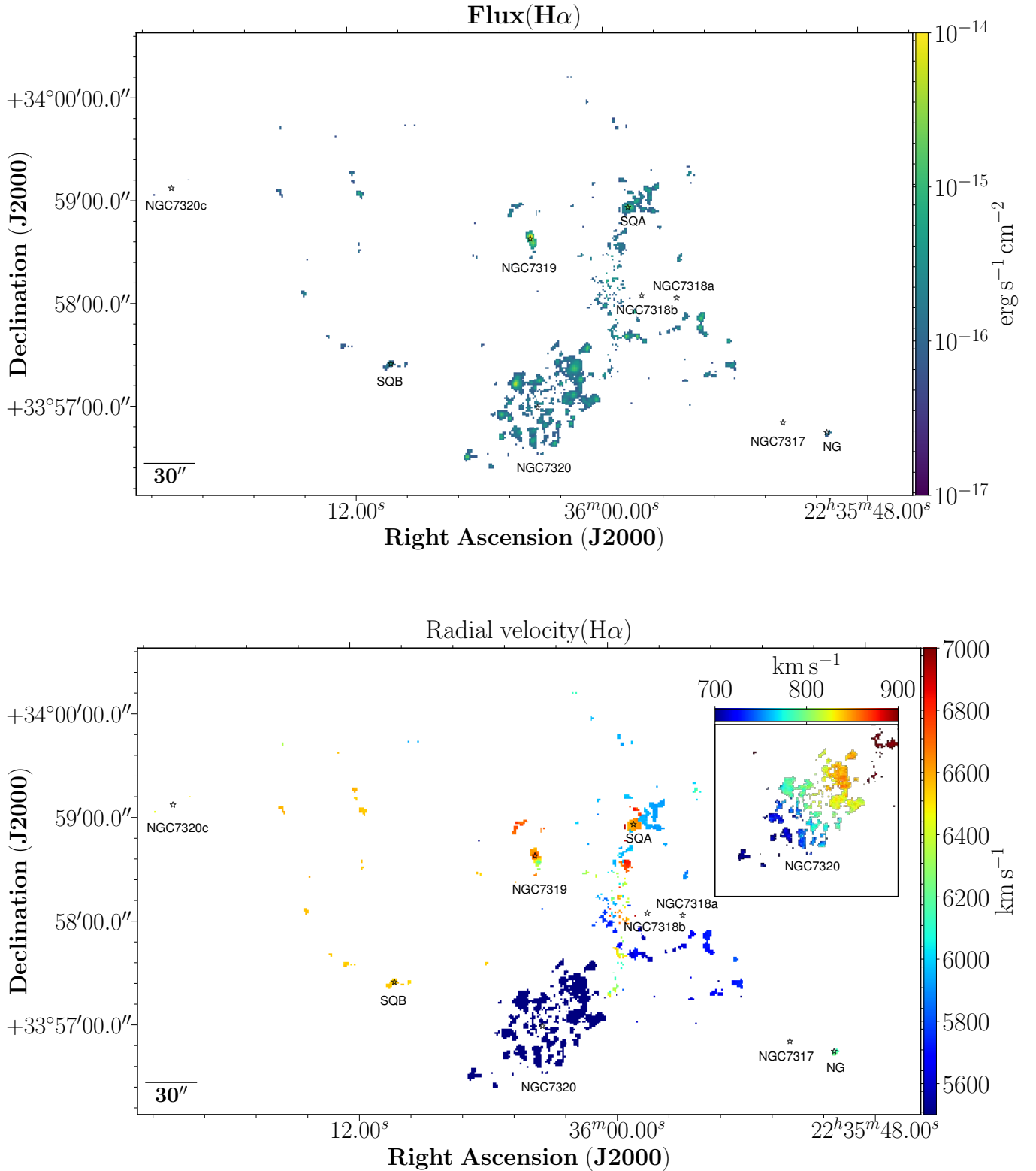

Fig. 3. *Top panel*: Hα flux map of SQ considering pixels with Hα contrast ≥5. *Bottom panel*: Hα radial velocity map of SQ considering pixels with contrast (Hα) ≥ 5. The inset plot in the right panel indicates the radial velocity map of NGC 7320, the foreground galaxy, with contrast (Hα) ≥ 5 (see the text for details). NG (new dwarf galaxy) indicates the position of the new dwarf galaxy in SQ (see Sect. 3.4).

emission region. We followed the same methodology as previously described. For SN1 we fitted the spectral line [O II]λ3727. For SN2 we fitted the lines Hβ and [O III]$\lambda\lambda$4959,5007 in the wavenumber range [19493,20746] cm^{-1} (assuming the theoretical relation [O III]λ4959/5007 = 0.333). The standard deviation

for the SN1 and SN2 filters (std$_{90}$) was derived as above. Figure 4 illustrates examples of the line fits for the SN1, SN2, and SN3 filters. All the line fluxes fitted in the SN1, SN2, and SN3 data cubes will be presented in a future paper (Duarte Puertas et al., in prep., Paper II).
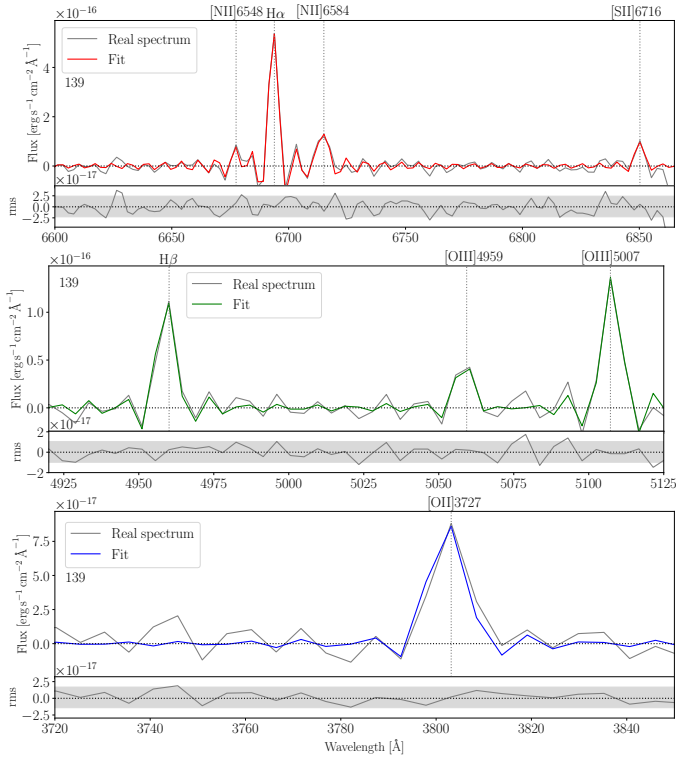
Fig. 4. Fitting example: spectra from region 139. In each *upper panel*, the grey line shows the real spectrum and the red, green, and blue coloured lines show the fit obtained with ORCS in the SN3, SN2, and SN1 filters, respectively. *Upper panels*: grey dotted lines show the location of the emission lines studied for this region. *Lower panels*: grey line shows the residual after the fit. The horizontal grey band indicates the 3σ scatter.

2.2.4. Complex kinematics spectral fitting of emission regions

The one-velocity-component spectral fitting procedure produced unsatisfactory results for a selection of emission regions. A close visual inspection of these fits showed complex kinematics, with large velocity dispersion for the emission regions associated with the AGN galactic nucleus of NGC 7319 and the shock region (see Fig. 3 lower panel). Taking into account our spectral resolution and the signal-to-noise ratio, we studied only two velocity components for those emission regions with the velocity components resolved, as follows:

The Hα, [N II]$\lambda\lambda$6548,6583, and [S II]$\lambda\lambda$6716,6731 emission lines of the spectrum of the SQ shock region were fitted simultaneously in the wavenumber range [14 820,15 021] cm^{-1} and with a sincgauss function. When one or both velocity components presented contrast in the Hα line lower than three, we assumed that they fit the criterion to be considered as one velocity component. Finally, for the rest of the emission lines ([O II]λ3727, Hβ, and [O III]$\lambda\lambda$4959,5007), we performed a two-component fit using the velocities and line widths derived from the Hα fit as input. We found 22 SQ Hα emission regions with line profiles that can be fit with two velocity components.

2.3. Sample of SQ Hα emission regions

Following the methodology described above, we found 209 candidate emission regions in the SQ field. However, in this work we only focus on those regions that belong to SQ (hereafter, "SQ

Hα emission regions") according to the following criteria: (i) the radial velocity of the region is within the radial velocity range of SQ (between ∼5600 and ∼7000 km s^{-1}); and (ii) at least one additional emission line besides Hα has been detected in the data cubes. According to this criteria, 175 SQ Hα emission regions were found. From these regions, 22 present broad Hα profiles that have been fit using two velocity components. There may be more than two velocity components, but for our spectral resolution, the residuals of the fit produced are found to be within a band of width 3 sigma rms of the defined continuum window. We selected the minimum number of components obtained, considering the resolution and the signal-to-noise ratio of our data cubes.

In Figs. 5 and 6 we show the sample of 175 SQ Hα emission regions found in this work. The location of the 15 extra Hα emitter regions presented in Table A.1. are also shown. In Table B.1 we present the catalogue of these SQ Hα emission regions. In Col. 1 the region name is presented, Col. 2 shows the RA and Dec coordinates, Cols. 3 and 4 show the radial velocity and the area, Col. 5 indicates the corresponding subzone. We add the information for NGC 7320c which is discussed in Sect. 3.4 (ID 1 in Table B.1). We have compared our results with the recent works by Konstantopoulos et al. (2014) and Iglesias-Páramo et al. (2012). From the 40 Hα emitting regions presented in Konstantopoulos et al. (2014), 34 have the same α, δ as our regions. Twenty-five of these regions can be directly compared since they present a single value of radial velocity. When compared with Iglesias-Páramo et al. (2012), which has lower spatial resolution, only six regions were identified (pointings M and S). The mean of the differences between our Hα radial velocities and the ones in these previous works, Δv, is $\Delta v = 1.1 \pm 14.9$ km s^{-1}, which is consistent to within the errors.

For the sake of the analysis of the sample, in the following we separate the SQ emission regions in two sub-samples: lower radial velocity sub-sample (LV) composed of those regions where the radial velocity $\leq$6160 km s^{-1} (for the two velocity components fit, the lowest radial velocity was considered); conversely, the higher radial velocity sub-sample (HV) is defined including all the regions with radial velocity >6160 km s^{-1} (for the two velocity components fit, the greatest radial velocity was considered). The nominal radial velocity of 6160 km s^{-1} was chosen as a limit value to highlight the discrete emission features associated with NI (NGC 7318B).

Figure 7 presents the different zones and subzones defined by the 175 SQ Hα emission regions (see below). In Fig. 8 we show the radial velocity versus RA diagram in the upper right panel; Dec versus radial velocity diagram in the upper right panel; and a three-dimensional view (i.e. RA – Dec – radial velocity diagram) of SQ Hα emission regions in the lower panel. From the three-dimensional information obtained considering Figs. 7 and 8, we have defined 12 zones and 28 subzones in SQ. We have divided the zones (and thus the subzones) in the following way: (i) YTT (e.g. Lisenfeld et al. 2002), so that north and south strands are respectively YTTN and YTTS, and NGC 7320c is the old intruder (OI); (ii) NGC 7319 (NGC 7319 nucleus, NGC 7319 "arm", north lobe); (iii) Hα "bridge"; (iv) high radial velocity strands, Hs (H1 and H2); (v) SQA (e.g. Xu et al. 1999); (vi) low radial velocity strands, Ls (L1, L2, L3, and L4); vii) shock strands, Shs (Sh1, Sh2, Sh3, and Sh4); (viii) north and south of SQA (NSQA and SSQA, respectively); (ix) tidal tail at north of NSQA (NW, e.g. Renaud et al. 2010); (x) NI (e.g. Moles et al. 1997) strands, NIs (NI1, NI2, NI3, NI4, and NI5); (xi) southern debris region (SDR, e.g. Fedotov et al. 2011); and (xii) NG (see Sect. 3.4). Also, the 15 extra Hα emitter regions
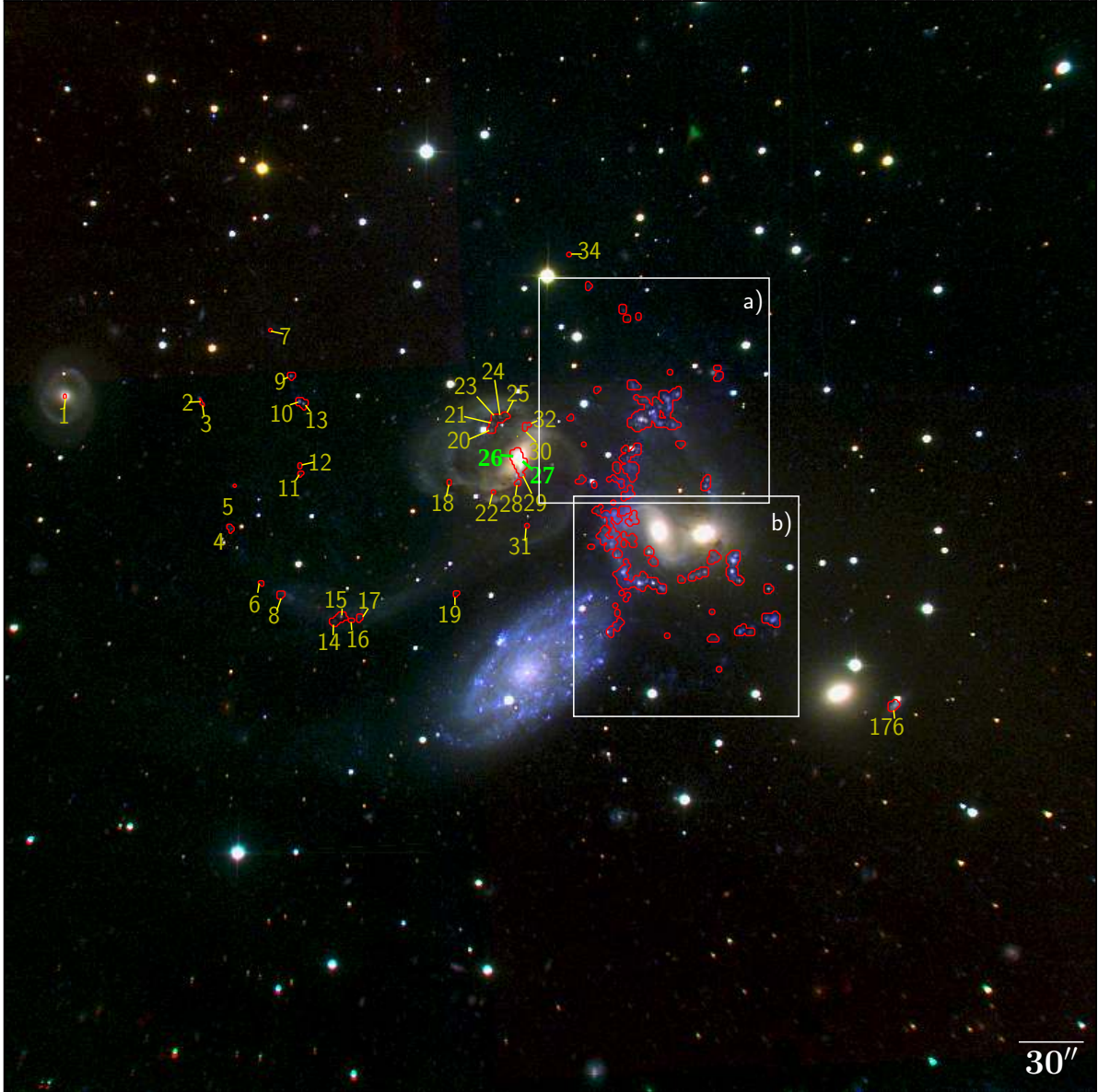
Fig. 5. SITELLE composite image from deep SN1, SN2 and SN3 data cubes of SQ. The red lines represent the Hα contours corresponding to all 175 SQ Hα emission regions defined in Sect. 2.3. The Hα regions from YTT, NGC 7319, NGC 7320c, and NG are labelled according to the nomenclature from Table B.1. Green and yellow labels identify the SQ Hα regions showing a broad and narrow line profile, respectively. A zoomed-in view of the areas marked with the white rectangles are shown in Fig. 6.

from Appendix A are shown. Section 3.3 explains in more detail the connections between each zone and subzone. For each zone a detailed study was made to understand better the kinematic and chemical processes acting on SQ (see Sect. 3 and Duarte Puertas et al., in prep., Paper II).

3. Results

3.1. Kinematical properties of SQ Hα emission regions

Figure 9 shows the radial velocity maps for the 175 SQ Hα regions. The SQ Hα regions have been catalogued in two velocity sets, LV and HV, according to the definitions given in Sect. 2.2. Traditionally, two velocity ranges were observed in the shock zone. However, Iglesias-Páramo et al. (2012) showed an additional velocity range in the shock region. As can be seen in Fig. 3, at least five different velocity ranges are clearly

distinguished, therefore, we can see two more velocity components. For low radial velocity components, two radial velocity ranges are shown: (i) $v = [5600-5900] \, \mathrm{km \, s^{-1}}$, associated with the NIs and the SDR; (ii) $v = [5900-6100] \, \mathrm{km \, s^{-1}}$, associated with the north of NSQA, SSQA, NW, and the Ls. For high radial velocity components, three radial velocity ranges are shown: (i) $v = [6100-6600] \, \mathrm{km \, s^{-1}}$, associated with the Shs, connecting the part of SQ with high radial velocities with the lower radial velocities; (ii) $v = [6600-6800] \, \mathrm{km \, s^{-1}}$, associated with the YTT, SQA, and AGN north lobe; (iii) $v = [6800-7000] \, \mathrm{km \, s^{-1}}$, associated with the Hs, the strands that connect Shs with SQA, and those regions of strands Sh3 and Sh4 (e.g. ID 56, 80b, 85, 89b, and 113) that are closest to the Hs strands.

The upper panel of Fig. 9 shows a radial velocity gradient that was found in the SQ Hα emission regions from NI2 to SSQA, NI2 to NI3, and NI2 to NI5, increasing northwards up to 6100 km s^{-1} (the minimum radial velocity is in region

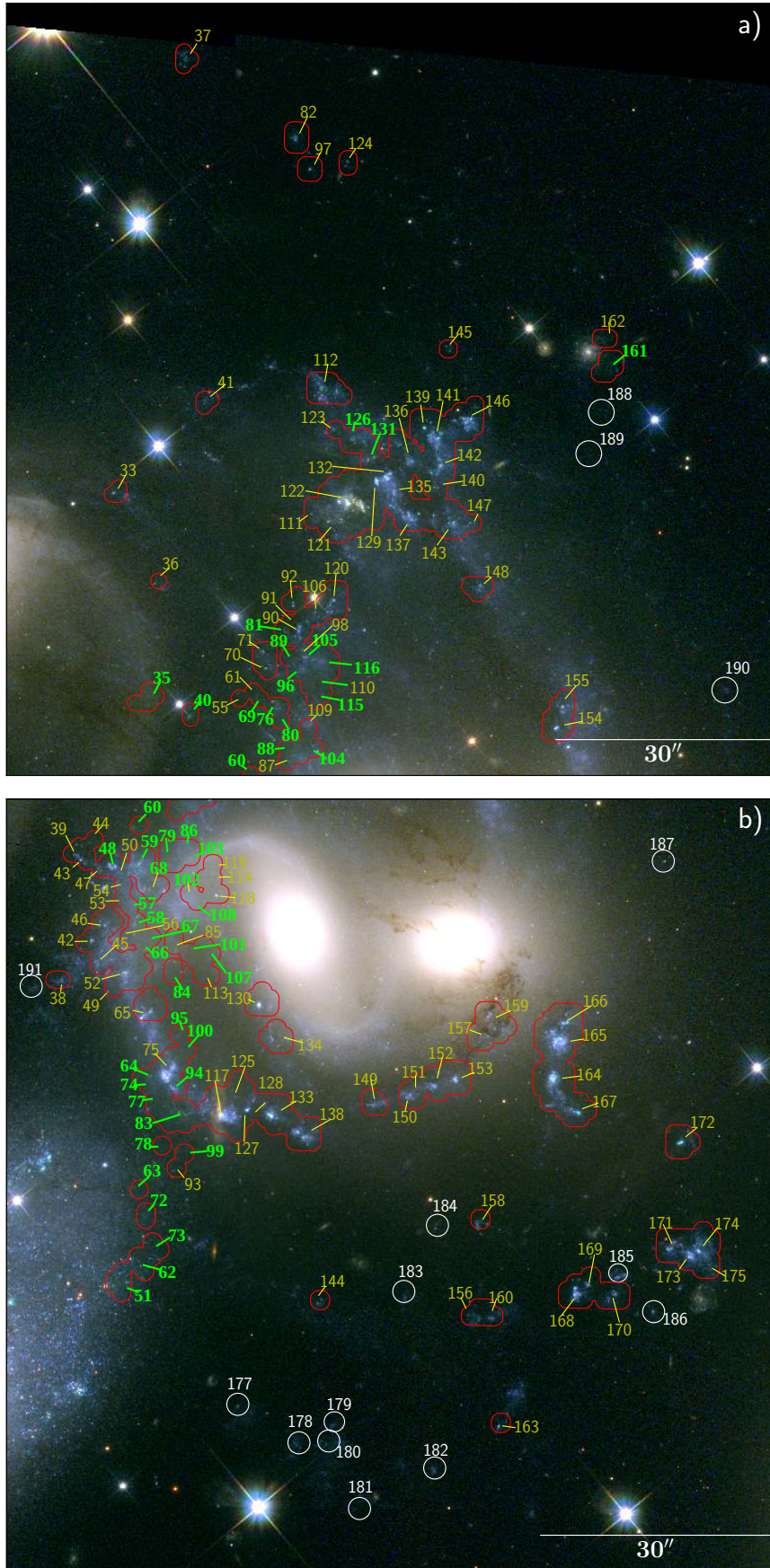**Fig. 6.** Zoomed-in view of image from *Hubble* Space Telescope Wide Field Camera 3, also known as HST/WFC3 (PID 11502, PI Keith S. Noll) showing regions *a* and *b* from Fig. 5. The red circles and labels are defined as in Fig. 5. White circles show the location of the 15 extra Hα emitter regions presented in Table A.1. Green and yellow labels identify the SQ Hα regions showing a broad and narrow line profile, respectively.

Fig. 7. Different systems of emission line objects defined here and indicated on SITELLE deep-colour image of SQ. Shown are the positions of YTTN and YTTS (magenta crosses and squares, respectively); NGC7319 nucleus, "arm", and north lobe (red triangles, squares, and circles, respectively); SQA (green crosses); Hs (H1: yellow circles; H2: yellow diamonds); Shs (Sh1: blue squares; Sh2: blue triangles; Sh3: blue circles; Sh4: blue crosses); Ls (L1: orange triangles; L2: orange circles; L3: orange crosses; L4: orange diamonds); NSQA and SSQA (violet squares and circles); NW (cyan triangles); NIs (NI1: brown squares; NI2: brown triangles; NI3: brown circles; NI4: brown crosses; NI5: brown diamonds); SDR (salmon stars); and NG (grey squares). In addition, the salmon unfilled stars show the position of the 15 extra Hα emitter regions in Appendix A from Table A.1.
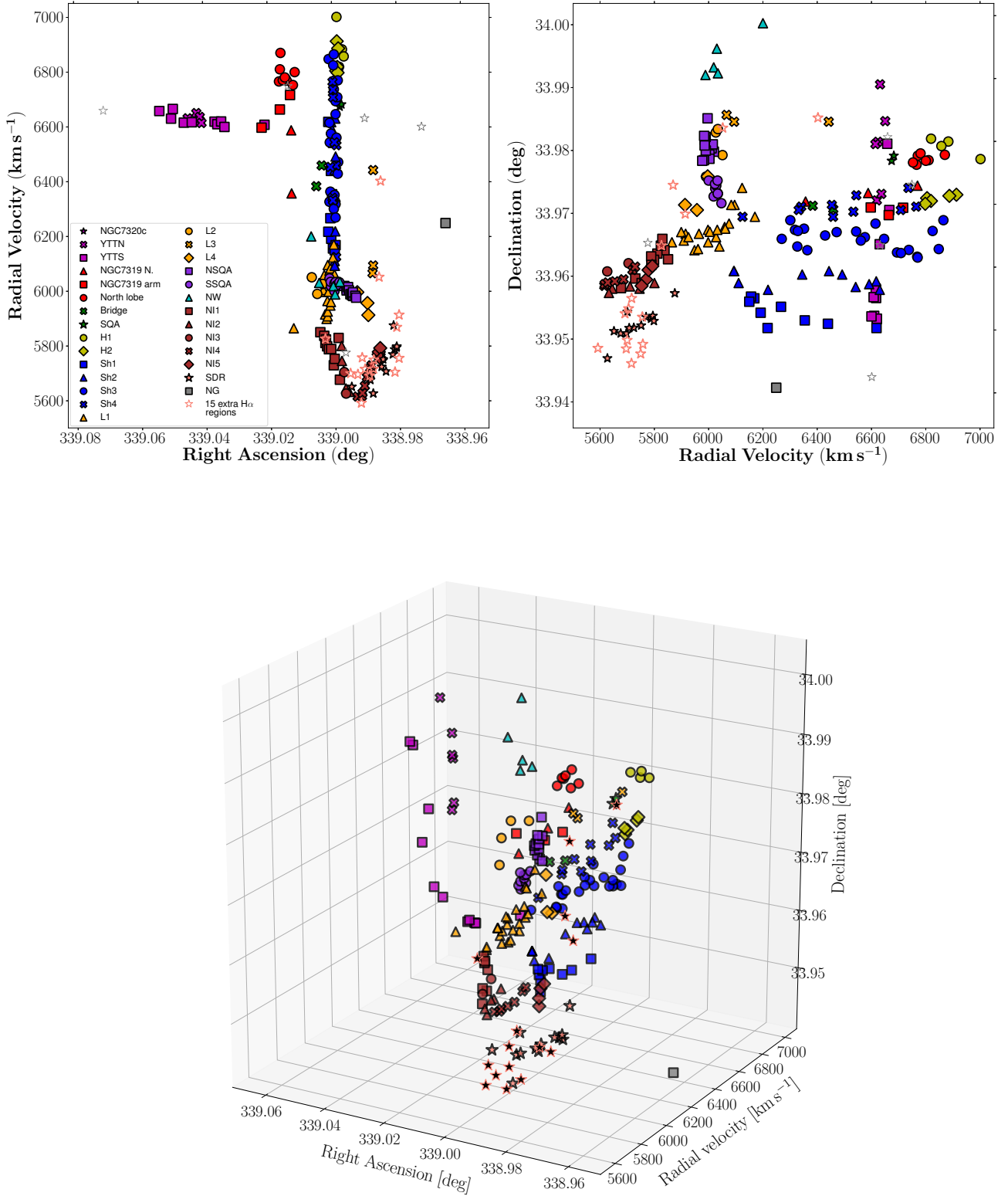
Fig. 8. *Upper left panel*: radial velocity versus RA diagram. *Upper right panel*: Dec versus radial velocity diagram. *Lower panel*: three-dimensional view of SQ Hα emission regions (RA, Dec, and radial velocity diagram). All the points in the figures have the same colours and markers as Fig. 7. In both *upper panels*, the nuclei of NGC 7320c, NGC 7319, NGC 7318B, NGC 7318A, and NGC 7317 are marked with an unfilled grey star.

149, radial velocity ∼5610 km s^{-1}). Located north of NSQA we can see the tidal tail NW with radial velocity ∼6000 km s^{-1}. According to the simulations from Renaud et al. (2010), NW could have been formed by the merger between NGC 7318B and NGC 7318A. We have no clear evidence of this, but we believe

that NSQA and SSQA have participated in this formation. This possible large-scale structure, which could be linked with the region 145 ($v = 5994$ km s^{-1}), is revealed. NI strands and SDR have lower radial velocities than ∼5900 km s^{-1}. Moreover, regions with radial velocities higher than 6160 km s^{-1} are presented in
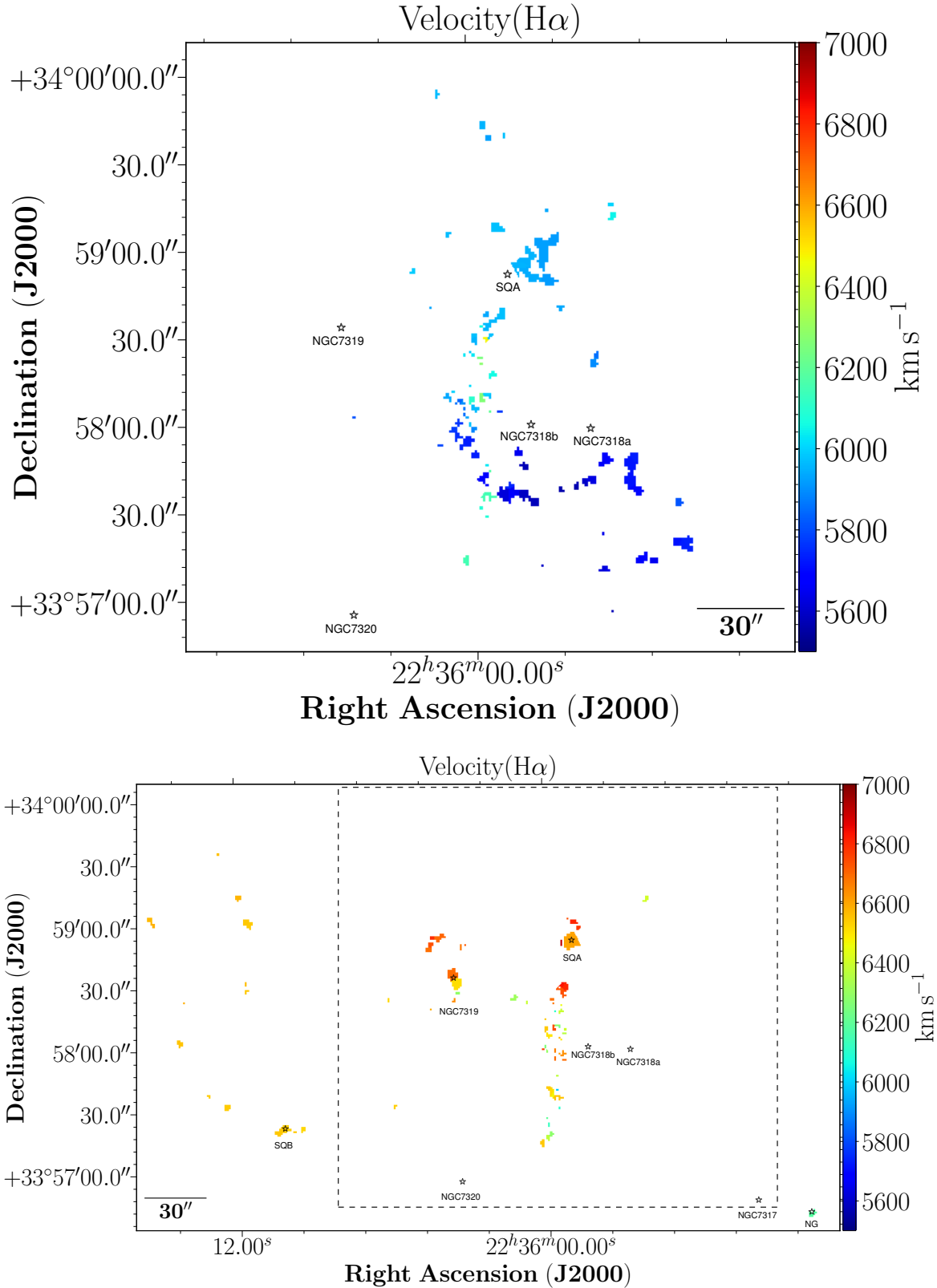
Fig. 9. SQ spatial map, colour-coded according to radial velocity of Hα for LV sample (*upper panel*) and HV sample (*lower panel*). The box in the *lower panel* indicates the zoomed zone shown in the *upper panel*.

Fig. 9 (lower panel). We detected several strands (Shs) that connect HV with LV parts covering a range of radial velocities from ~6100 to ~6600 km s^{-1}. SQA has radial velocity ~6670 km s^{-1}. Additionally, the north lobe has radial velocities from 6750 to 6870 km s^{-1}. We found two SQ regions in the Hα "bridge" (radial velocity ~6400 km s^{-1}, see Sect.3.3 for more information). The strands H1 and H2 connect Shs with SQA. The radial velocity and the Dec increase in H1 up to region 111 (radial velocity
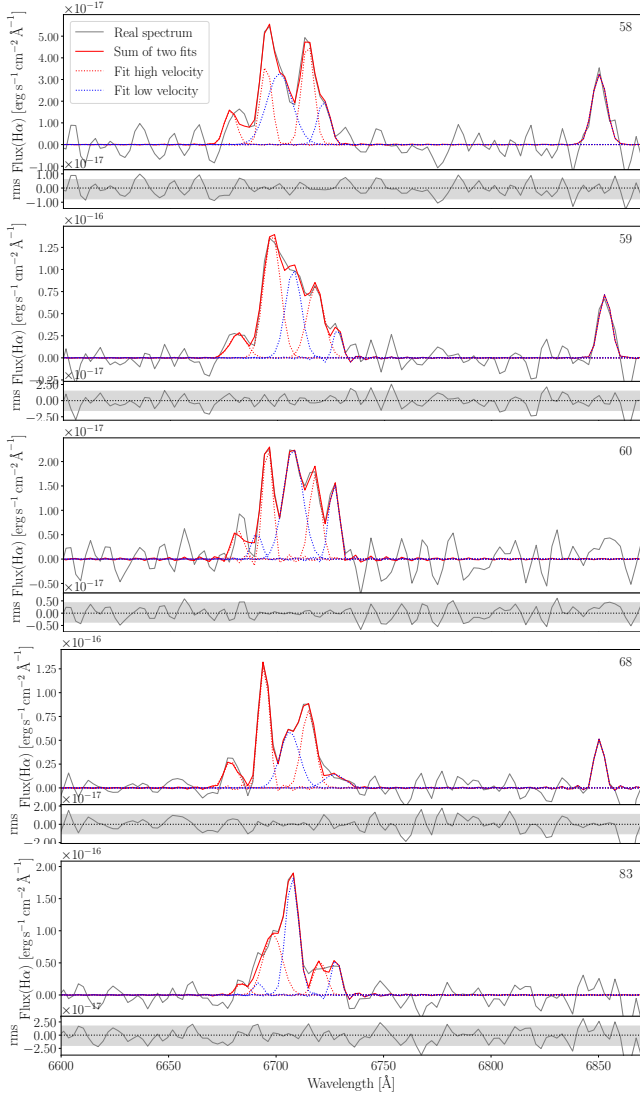
Fig. 10. *From top to bottom*: examples of the line fits from regions 58, 59, 60, 68, and 83 with a broad line profile. In each *upper panel*, the grey line shows the real spectrum, and the red and blue dotted lines correspond to the fit of the low and high velocity components. The red solid line shows the sum of the two velocity component fits. The name of the region is indicated in each *upper panel* (*top right*). *Lower panels*: grey line shows the residual after the fit. The horizontal grey band indicates the 3σ scatter.

Fig. 11. Same as Fig. 10 but for region 161.

Fig. 12. Integrated spectra from large scale shock region in SN3, SN2, and SN1 data cubes. The black and red vertical dashed lines show the position of the emission lines studied at Hα radial velocities of $6000\,\mathrm{km\,s^{-1}}$ and $6600\,\mathrm{km\,s^{-1}}$, respectively.

$\sim$7000 km s^{-1}). From region 111 to SQA (in H2) the radial velocity decreases. The NGC 7319 nucleus (regions 26, 27, and 29) shows radial velocities between $\sim$6350 and 6760 km s^{-1} as a result of the outflow from the nucleus (Rodríguez-Baras et al. 2014). It is noteworthy that the NGC 7319 "arm" has regions with radial velocities from $\sim$6710 (in region 28) to $\sim$6600 km s^{-1} (in region 18). We do not discard the possibility that it is produced by the interaction between NGC 7319 and another galaxy and it will remain as a conatus of tidal tail. The YTT has an average radial velocity of $\sim$6620 km s^{-1}. YTT increases its radial velocity as we move away from NGC 7319. Another interesting finding is the NG (see Sect. 3.4).

3.2. Regions with broad line profile

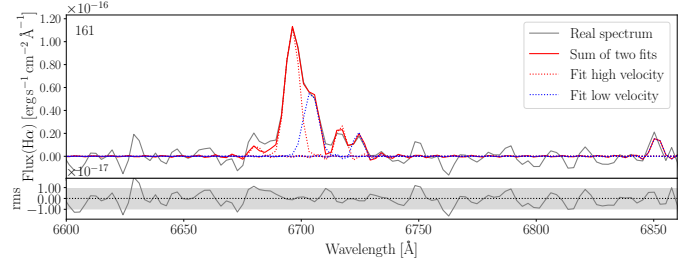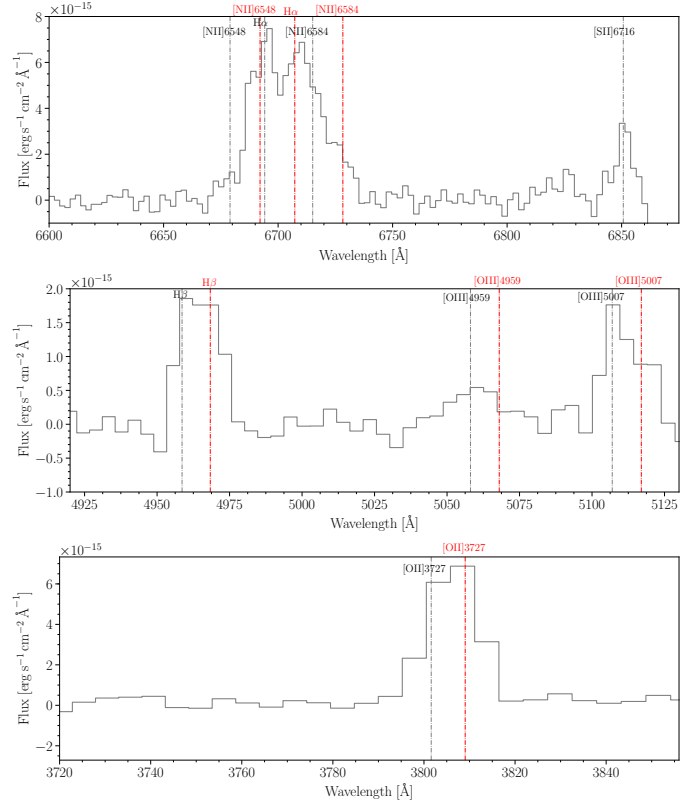As we can see in Sect. 2.3, SQ presents regions with broad and narrow line profiles. The regions showing a broad line profile are located in the LSSR, the AGN nucleus of NGC 7319, and the L1 and L4 zones. In Fig. 10 we show several examples of these individual regions (noted as ID 58, 59, 60, 68, 83 in Table B.1) across the LSSR, and their corresponding fits using two sincgaussian functions, as explained in Sect. 2.3. A close visual inspection has also been carefully performed of all the fits of the broad line profile.

In Fig. 11 we present the broad Hα profile we found for region 161 located in the L4 area, a somewhat outlying zone (see Fig. 7), and its two velocity component fits. As far as we know, this broad profile is presented here for the first time for region 161. It is tempting to associate this broad profile region with a nearby secondary maximum apparent in the X-Ray maps of Trinchieri et al. (2005). However, the precise nature and the excitation of this gas still has not been ascertained.

In order to show the wide range of velocities encompassed within LSSR, its integrated emission is presented in Fig. 12 in the SN1, SN2, and SN3 filter windows. To obtain these
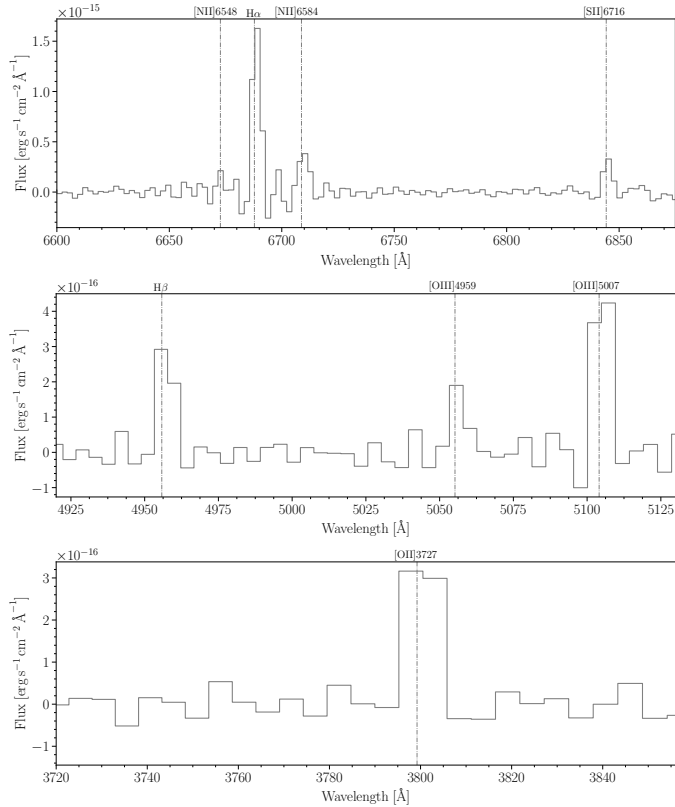
Fig. 13. Integrated spectra from SQ Hα region 164 in SN3, SN2, and SN1 data cubes.

spectra, we considered all the Hα emission detected (binning 6×6 and contrast ≥ 2) with Hα radial velocities $\geq 5000 \, \text{km s}^{-1}$ within a rectangle centred on the coordinate RA = 339 deg and Dec = 33.966 deg, with a width of $\Delta\text{RA} = 27.786$ arcsec and a height of $\Delta\text{Dec} = 99.512$ arcsec (defined according to the definition of the flux, as determined in the next section). As expected, the integrated spectra from LSSR show broad lines and several predominant peaks (e.g. Hα and [N II]λ6584). For illustrative purposes, these can be compared with a typical narrow-lined Hα emission region (i.e. ID 164; Fig. 13).

3.3. Unveiling low surface brightness Hα emission

In order to detect the low surface brightness Hα emission regions, we produced a deep overview of all the Hα emission of the SQ system in Fig. 14. This was produced using a binning 6×6, contrast (Hα) ≥ 2, and radial velocities in the range of the SQ, in order to increase the detectability of the low surface brightness emission, as explained in Sect. 2.2. From a statistical analysis of our Hα flux measurements, we find that below a value of Hα flux per pixel of $6 \times 10^{-18} \, \text{erg s}^{-1} \, \text{cm}^{-2}$ we can distinguish a very low surface brightness Hα component besides the SQ Hα emission regions measured. The upper right panel of Fig. 14 shows a zoomed-in view of the LSSR, whereas the lower panels, as in Fig. 8, shows an overlapped view of the symbols corresponding to the very low surface brightness regions detected with the SQ Hα emission regions found in Sect. 2.3. This low surface brightness gas emission represents different components spread throughout the whole system. This gives us important information about the connections between the different SQ zones (see Sect. 2.3) and helps us to better understand the complexity of SQ.

At lower radial velocities, $v \leq 6160 \, \text{km s}^{-1}$ (see lower panels in Fig. 14), we observe at least two subsystems that were probably in collision. On one hand, NI (brown symbols)[4] colliding with the debris field in the shock path at L1 strand (orange triangles), on the other hand, the interaction between NSQA and SSQA (violet squares and circles, respectively). While the collision between NI and the debris field in the LSSR appears to be ongoing at this moment (e.g. Iglesias-Páramo et al. 2012), our observations indicate that the interaction between NSQA and SSQA has had at least one previous collision. Several strands of ionised gas emerging from NSQA are found here: to the north of NSQA a tidal tail, NW (cyan triangles) is indicated, while on the right we see the strand L3 (which increases towards higher radial velocities, $\sim6470 \, \text{km s}^{-1}$, orange crosses) and the strand L4 (that goes southwards and could link with NI, orange diamonds). The strand L2 (orange circles) connects NSQA with SSQA, which reinforces the idea that NSQA and SSQA have had at least one previous interaction. The strand L1 joins the system formed by NSQA and SSQA with NI1. We must bear in mind that the majority of the regions from the strand L1 are compatible with fast shocks without precursor for solar metallicity and low density, with velocities between $175 \, \text{km s}^{-1}$ and $300 \, \text{km s}^{-1}$ from Allen et al. (2008) models (Duarte Puertas et al., in prep., Paper II).

At intermediate radial velocities (i.e. from $v \sim 6160$ to $\sim6660 \, \text{km s}^{-1}$), several strands can be seen connecting Hs with Ls through the Shs strands (namely Sh1, Sh2, Sh3, and Sh4 represented by blue squares, triangles, circles, and crosses, respectively; see Figs. 8, upper right panel, and 14). It seems clear that this gas is a product of the interaction processes that occurred in SQ between NI and the debris field in the shock, although understanding these processes becomes complex. We also see at radial velocities $\sim6360 \, \text{km s}^{-1}$ Hα flux that connects the shock (Sh4 strand) with NGC 7319, into an Hα "bridge" (green crosses). This bridge has also been observed at other wavelength ranges (e.g. molecular hydrogen bridge detected: Cluver et al. 2010; Guillard et al. 2010; Appleton et al. 2013, 2017). In Fig. 14 (lower left panel) we can appreciate that this connection extends several hundred km s^{-1}.

At higher radial velocities, $v > 6660 \, \text{km s}^{-1}$ we distinguish several gas strands. On one hand, from the NGC 7319 nucleus (red triangles) an outflow emerges, from radial velocities $\sim6760 \, \text{km s}^{-1}$ to $\sim6350 \, \text{km s}^{-1}$, in agreement with Rodríguez-Baras et al. (2014). On the other hand, the NGC 7319 "arm" (red squares) emerges up to radial velocities $\sim6600 \, \text{km s}^{-1}$ westward towards YTT (magenta crosses and squares). The AGN north lobe zone (red circles) covers velocities higher and lower than that of the NGC 7319 nucleus ($\Delta v \sim 200 \, \text{km s}^{-1}$). The right part of the north lobe seems to reach the NGC 7319 "arm". Conversely, in the shock part we see the strands H1 and H2 (yellow circles and triangles). These strands connect Shs with SQA (green stars) in the following ways: (i) from Shs (radial velocity $\sim6660 \, \text{km s}^{-1}$) to the most distant region detected (region 111, radial velocity $\sim7000 \, \text{km s}^{-1}$) through the strand H2; and (ii) from region 111 to SQA (radial velocity $\sim6670 \, \text{km s}^{-1}$) through strand H1.

We fail to detect ionised gas neither in the old tail, nor in the vicinity of NGC 7318A in agreement with Moles et al. (1998), nor in NGC 7317 in agreement with Duc et al. (2018). Neither do we find evidence that there is a gas connection between the NGC 7319 north lobe and SQA. Finally, we do not detect gas connecting the LSSR and NI5, nor in SDR (salmon stars).

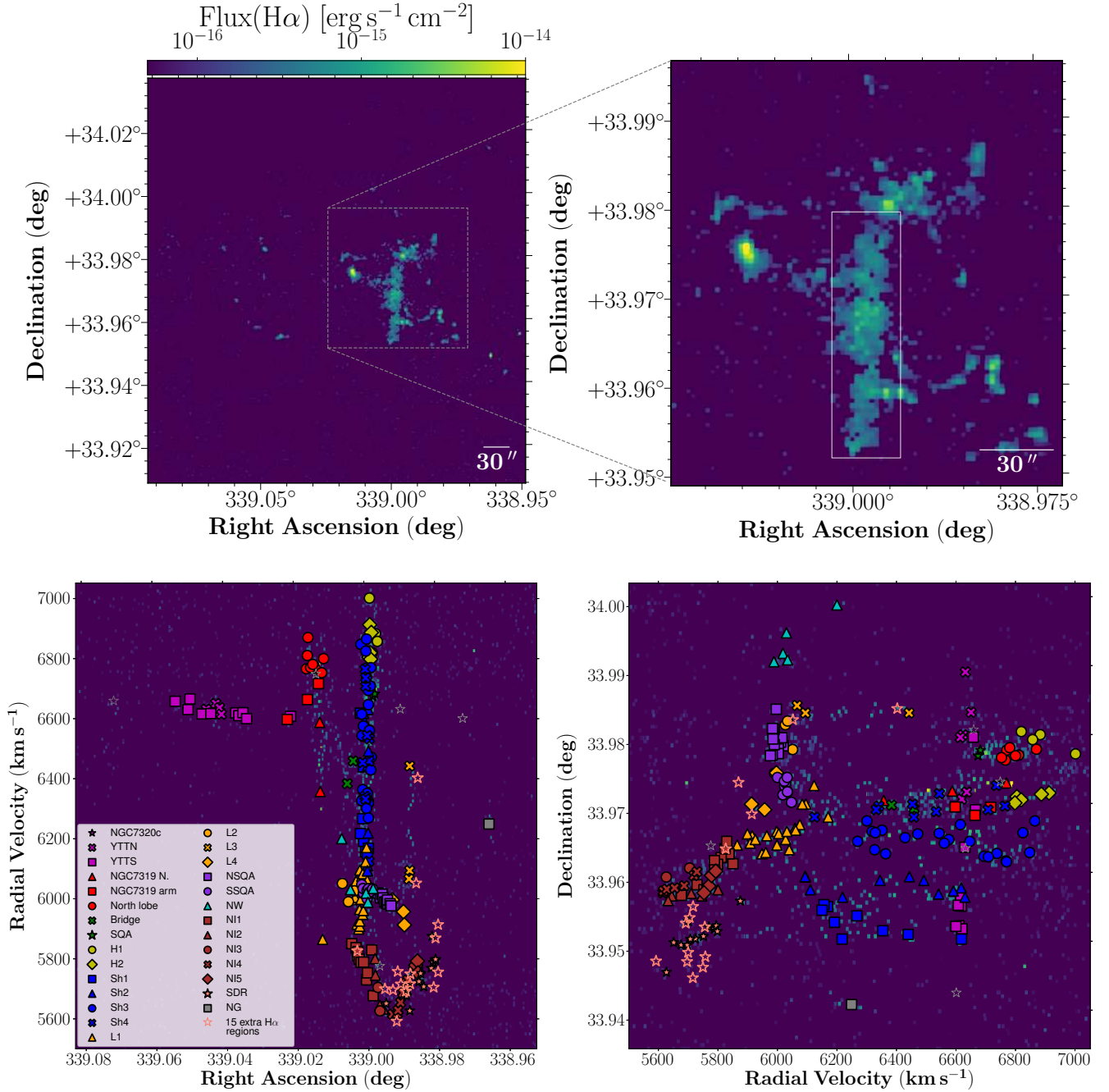[4] All symbols referenced in this subsection come from Fig. 7.

Fig. 14. Hα flux spatial map of entire SQ (*upper left panel*), Hα flux spatial map zoomed in to shock region (*upper right panel*). *Lower left panel*: radial velocity versus RA diagram and the *lower right panel* shows Dec versus radial velocity diagram. All the points in the *lower panels* of the figures have the same colours and markers as Fig. 7. The white rectangle centred on LSSR is overplotted with a solid line in the *upper right panel*. This rectangle is centred on the coordinate RA = 339 deg and Dec = 33.966 deg, with a width of ΔRA = 27.786 arcsec and a height of ΔDec = 99.512 arcsec.

3.4. The other galaxies in SQ

In most articles that study SQ, the galaxies that are studied in detail are NGC 7317, NGC 7318a, NGC 7318b, and NGC 7319, as well as NGC 7320. In this work, thanks to the large SITELLE FoV, we were able to add to the study of the galaxy NGC 7320c (the OI) and the NG. In Figs. 15 and 16 we present the spatially resolved Hα flux and radial velocity maps for NG and NGC 7320c, respectively.

We detect Hα emission in NG. This, combined with the fact that NG is extended and presents a galactic rotation of $\pm 60 \,\mathrm{km\,s^{-1}}$ as shown in Fig. 15 (e.g. Swaters et al. 2002, Westmoquette et al. 2013), indicates that NG is consistent with a dwarf galaxy that will end up interacting with the SQ system in the future, similar to M 82 (according to the Tully-Fisher relation). A more detailed study has been made for NG. In Fig. 15 we show the Hα flux (left panel) and the radial velocity map (right panel) of NG. The inner panel shows the *Hubble* Space Telescope optical imaging of NG. The velocity gradient is clearly seen from the south to the north ($v \sim 6300$ to $\sim 6150 \,\mathrm{km\,s^{-1}}$). As we can see in Table B.1, region 176, the average radial velocity for NG is $6246 \,\mathrm{km\,s^{-1}}$.
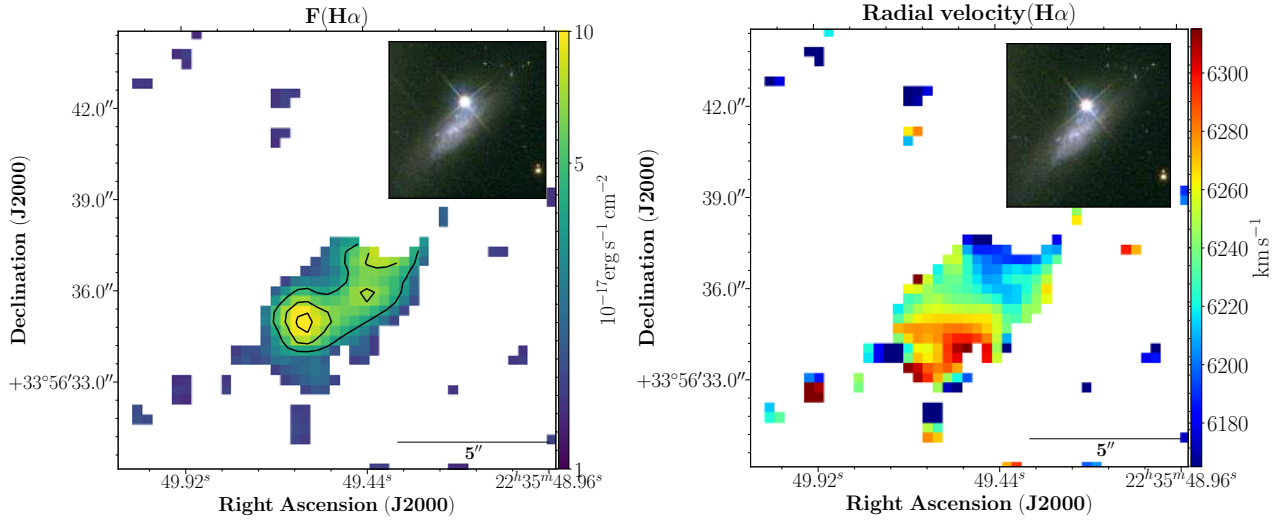
Fig. 15. NG Hα flux spatial map (*left panel*) and Hα radial velocity map (*right panel*). *Inner panels*: HST/WFC3 optical imaging for NG. The black contours are 1×10^{-17}, 4×10^{-17}, and 7×10^{-17} erg s^{-1} cm^{-2}.
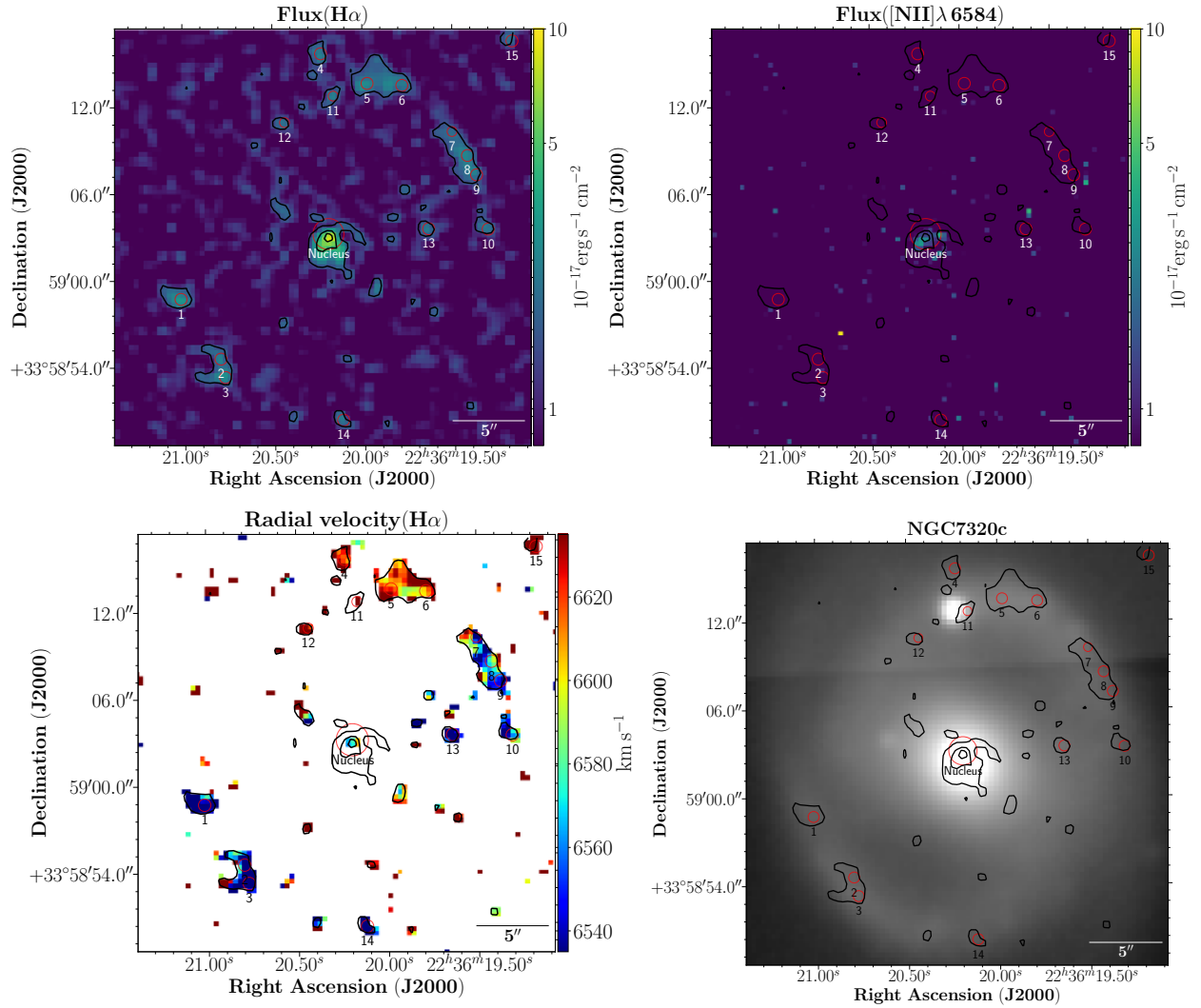
Fig. 16. NGC 7320c Hα flux spatial map (*upper left panel*), [N II]λ6584 flux spatial map (*upper right panel*), Hα radial velocity map considering pixels with contrast (Hα) ≥ 2.5 (*lower left panel*), and deep image from SN2 filter (*lower right panel*). Red circles represent the locations of the NGC 7320c nucleus and 15 Hα emission regions from its spiral arms. The black contours are 1.5×10^{-17}, 4×10^{-17}, and 7×10^{-17} erg s^{-1} cm^{-2}.
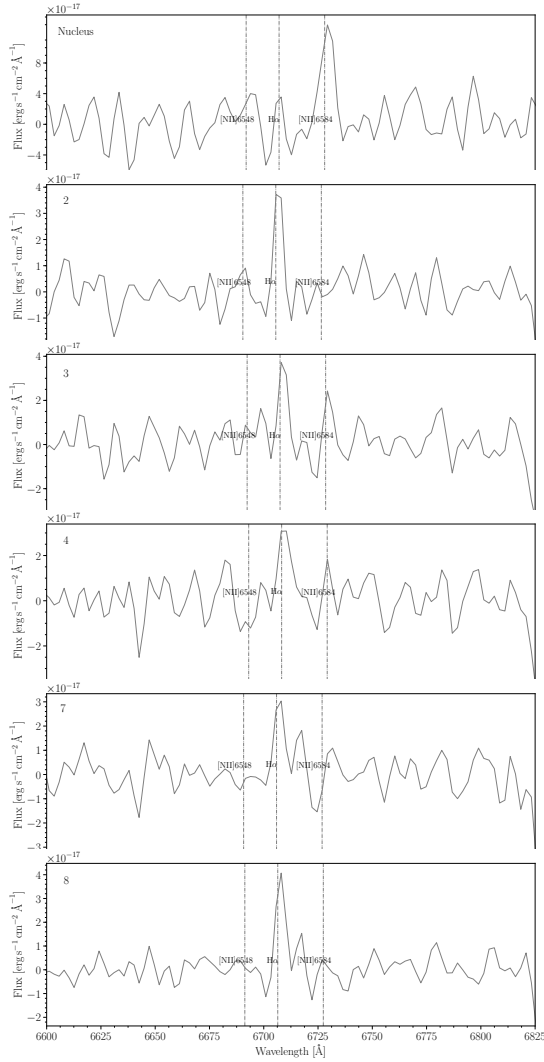
Fig. 17. Spectra from NGC 7320c nucleus, and several Hα regions in its galactic disc. Shown from *top to bottom* are the NGC 7320c galactic nucleus and regions 2, 3, 4, 7, and 8 (see Fig. 16). The black vertical dashed lines show the position of the emission lines studied for the SN3 filter at an Hα radial velocity of ~6590 km s⁻¹.

In Fig. 14 (upper left panel) we show the low surface brightness Hα emission in the strongly stripped galaxy NGC 7320c. Past interaction processes have stripped much of the gas in NGC 7320c. For a better understanding of this galaxy, we studied the Hα and [N II]λ6584 fluxes for this galaxy. Figure 16 shows the Hα flux map (upper left panel), the [N II]λ6584 flux map (upper right panel), the Hα radial velocity map (lower left panel), and the deep image from the SN2 filter (lower right panel) for NGC 7320c. In this figure, we see the presence of Hα and [N II]λ6584 emission in the galactic nucleus, and Hα emission in several regions located in the spiral arms. Figure 17 shows examples of spectra for several regions with Hα emission found in NGC 7320c. Observing the fit for the galactic nucleus emission line (see upper panel in Fig. 17), we ascertain that the spectrum has an AGN profile (and found a strong emission of [N II]λ6584). We barely observe [N II]λ6584 emission (or it may be very small) in the rest of the regions located in the NGC 7320c spiral arm. The radial velocity map covers a range of radial velocities from ~6540 to ~6640 km s⁻¹.
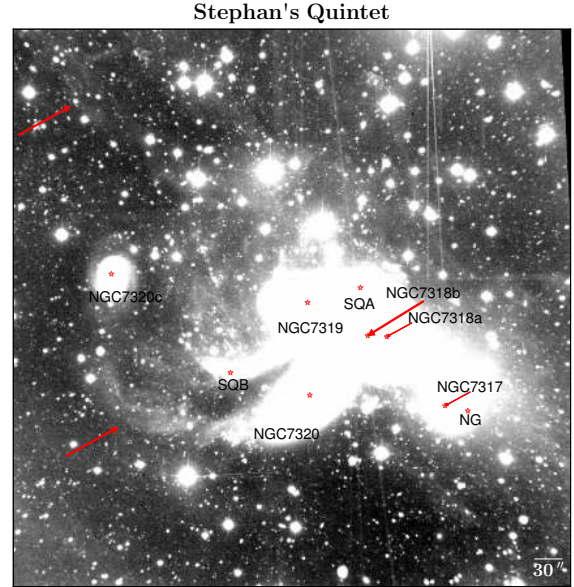

Fig. 18. Deep imaging from SN2 filter of SQ. This image displays the full extension of the entire system, including the diffuse ionised gas halo around the SQ. The most relevant components are indicated by their labels and red arrows. See the text for details.

4. Discussion and final remarks

A sample of 175 SQ Hα regions, 22 of them with two velocity components, has been made according to the following criteria: (i) the radial velocity of the region is within the range of SQ (between ~5600 and ~7000 km s⁻¹); (ii) the detection of at least one additional emission line besides Hα. Additionally, in Appendix A we add the relevant information of 15 extra Hα emitters that we have found in the southern debris region, close to NI, and to the west of SQ (regions from 177 to 191 in Table A.1).

Two large groups of radial velocities were found (radial velocities ≤6160 km s⁻¹ and >6160 km s⁻¹). We found five radial velocity components in SQ: (i) $v = [5600−5900]$ km s⁻¹, associated with NI and SDR; (ii) $v = [5900−6100]$ km s⁻¹, associated with the NSQA and SSQA and the strands that are connected to these zones; (iii) $v = [6100−6600]$ km s⁻¹, associated with the strands located in the shock; (iv) $v = [6600−6800]$ km s⁻¹, associated with YTT, SQA, NGC 7319, and the north lobe; and (v) $v = [6800−7000]$ km s⁻¹, associated with the strands that connect the shock with SQA.

When considering a contrast (Hα) ≥ 2 and binning 6 × 6, we do not detect gas in the old tail, in the vicinity of NGC 7318A nor in NGC 7317. We also do not have evidence that there is any connection between (i) the north lobe in NGC 7319 and the left side of SQA; or (ii) the shock and the right part of NI nor SDR. Conversely, we find a link between the shock and the NGC 7319 AGN nucleus (Hα bridge). This bridge was detected in other wavelengths (e.g. Iglesias-Páramo & Vílchez 2001; Sulentic et al. 2001; Trinchieri et al. 2005; Cluver et al. 2010; Guillard et al. 2010, 2012; Appleton et al. 2013, 2017).

A region of remarkable line emission is located between NGC 7319 and the NI galaxy (NGC 7318B). A rectangular area has been defined (see Sect. 3.2, shown in Fig. 14) to include this emission which is associated with the LSSR. This has allowed us to investigate the complex kinematical nature of this emitting gas, making use of detailed spatially resolved multi-sincgaussian fitting. The LSSR has revealed a rich knotty
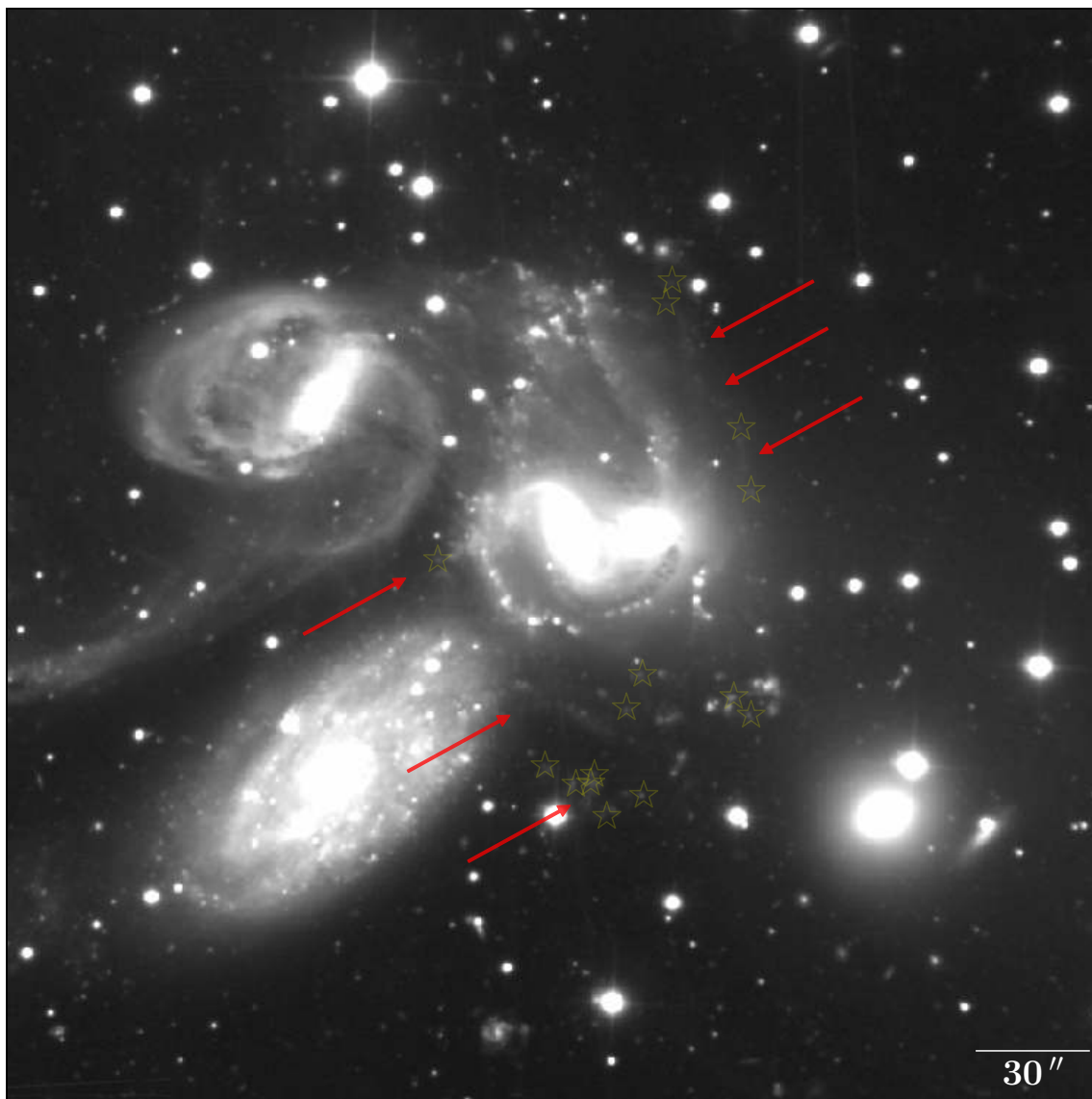
Stephan's Quintet

Fig. 19. Deep imaging from SN2 filter of SQ. Red arrows point out the possible outer structures that can be connected. The yellow stars show the location of the 15 extra Hα emitter regions presented in Table A.1.

substructure, spatially distributed, and also a set of kinematical properties of the Hα emitting knots. These knots show line profiles that have been fitted by two sincgaussian functions, with central velocities clustering around two main radial velocity values ($\sim$6000 km s^{-1}, $\sim$6600 km s^{-1}), and a different broadness in each case. Overall, taking into account: (i) an oblique interaction over a large region, and new and preceding gas (e.g. O'Sullivan et al. 2009; Lesaffre et al. 2013; Appleton et al. 2017); and (ii) that the gas is excited by shocks (corresponding to a shock radial velocity $\sim$300 km s^{-1} according to Allen et al. 2008, see Duarte Puertas et al., in prep., Paper II), we suggest that a variety of interaction processes occurred previous to the intrusion of NI in the main group. We found sub-structures $\sim$400 pc or larger in size, typical of giant HII extragalactic regions.

A possible outermost tail of Hα emitting regions is suggested here, which would be in agreement with Renaud et al. (2010). We provide an observational clue of this prediction. We found that this tidal tail connects with NSQA (reg 145). Other

strands connected with NSQA have been found: (i) the L2 strand that connects NSQA and SSQA; (ii) the L3 strand that connects NSQA with region 161 up to radial velocities $\sim$6470 km s^{-1}; and (iii) the L4 strand that connects NSQA with regions 154 and 155. This last connection could be extended up to the NI5 strand according to the diffuse gas show in the low surface brightness gas emission.

From our sample of SQ Hα emission regions we have studied the region 176 (i.e. NG) in detail (see Sect. 3.4). This region was previously observed by Torres-Flores et al. (2009; see their Fig. 14, ID 35) and by Rodríguez-Baras et al. (2014). In this paper we have made a spatially resolved study of the Hα radial velocity and Hα flux in this region. The data points out that this region is in fact a dwarf galaxy with a velocity gradient across its disc ($\pm$60 km s^{-1}, see Fig. 15), which was not considered by Rodríguez-Baras et al. (2014). These authors found an age of $\sim$10^{10} yr for 80% of the stellar mass in this region, assuming that this region is a star cluster separated from a galaxy by some

previous interactions. According to the Tully-Fisher relation, we found that NG would be similar to M 82. Additionally, we found Hα emission in the NGC 7320c galactic disc and a significant presence of broad [N II]λ6584 emission in the NGC 7320c nucleus. This leads us to propose that NGC 7320c hosts an AGN (see Fig. 17).

A panoramic view of the full extent of the low surface brightness emission of the SQ is illustrated in Fig. 18, which shows a deep imaging of SQ obtained from the SITELLE SN2 filter. This figure displays the full extension and complexity of the entire system (including the diffuse ionised gas halo around the SQ, the old tail, the halo around NGC 7317, and a conspicuously low surface brightness extension to the north-east of the whole system). For details, the reader is referred to the recent work by Duc et al. (2018), which offers an interesting study of the complete system.

Figure 19 shows the deep image from the SN2 filter. In this figure, we suggest a possible tidal structure (delineated by an outer rim to the north-west of NGC 7318B/A) with diffuse gas emission that could connect the south part of L3 and NSQA with NI4, NI5, and SDR (marked by a green arrow). The detection of the 15 additional low surface brightness Hα emission regions (i.e. IDs from 177 to 191 in Table A.1, located in: SDR, close to NI, and to the west of SQ) with the expected radial velocities in this zone ($\sim$5600 to $\sim$5900 km s^{-1}) has allowed us to support this possible connection. This outer rim is almost parallel with another inner rim (i.e. strand L4) that shows Hα emitting regions. Conversely, we do not discard the possibility of a connection between NI1 (i.e. region 38) and the left side of SDR going behind NGC 7320 (indicated by red arrows). Also this interaction could be supported by the existence of region 31 ($v \sim 5860$ km s^{-1}) presenting the same radial velocity as the strand NI1 some 13 kpc away to the east. The interaction suffered, which might explain these rims, appears complex, although we believe that it must have been produced by the interaction between NI and the group. The large-scale outer rim winding the NGC 7318B/A system clockwise north-west to south-east has been highlighted in continuum and from Hα. This structure may be reminiscent of a previously proposed scenario for SQ as a sequence of individual interactions (Renaud et al. 2010). Further observations are needed with higher spectral resolution to distinguish the complex kinematics that is taking place in the LSSR.

References

Allen, R. J., & Hartsuiker, J. W. 1972, Nature, 239, 324
Allen, M. G., Groves, B. A., Dopita, M. A., Sutherland, R. S., & Kewley, L. J. 2008, ApJS, 178, 20
Appleton, P. N., Xu, K. C., Reach, W., et al. 2006, ApJ, 639, L51
Appleton, P. N., Guillard, P., Boulanger, F., et al. 2013, ApJ, 777, 66
Appleton, P. N., Guillard, P., Togi, A., et al. 2017, ApJ, 836, 76
Astropy Collaboration (Robitaille, T. P., et al.) 2013, A&A, 558, A33
Burbidge, E. M., & Burbidge, G. R. 1961, ApJ, 134, 244
Cluver, M. E., Appleton, P. N., Boulanger, F., et al. 2010, ApJ, 710, 248
de Mello, D. F., Urrutia-Viscarra, F., Mendes de Oliveira, C., et al. 2012, MNRAS, 426, 2441
Drissen, L., Martin, T., Rousseau-Nepton, L., et al. 2019, MNRAS, 485, 3930
Duc, P.-A., Cuillandre, J.-C., & Renaud, F. 2018, MNRAS, 475, L40
Fedotov, K., Gallagher, S. C., Konstantopoulos, I. S., et al. 2011, AJ, 142, 42
Gallagher, S. C., Charlton, J. C., Hunsberger, S. D., Zaritsky, D., & Whitmore, B. C. 2001, AJ, 122, 163
Grandmont, F., Drissen, L., Mandar, J., Thibault, S., & Baril, M. 2012, in Ground-based and Airborne Instrumentation for Astronomy IV, SPIE Conf. Ser., 8446, 84460U
Guillard, P., Boulanger, F., Pineau Des Forêts, G., & Appleton, P. N. 2009, A&A, 502, 515
Guillard, P., Boulanger, F., Cluver, M. E., et al. 2010, A&A, 518, A59
Guillard, P., Boulanger, F., Pineau des Forêts, G., et al. 2012, ApJ, 749, 158
Heida, M., Jonker, P. G., Torres, M. A. P., & Mineo, S. 2012, MNRAS, 424, 1563
Hunter, J. D. 2007, Comput. Sci. Eng., 9, 90
Hwang, J.-S., Struck, C., Renaud, F., & Appleton, P. N. 2012, MNRAS, 419, 1780
Iglesias-Páramo, J., & Vílchez, J. M. 2001, ApJ, 550, 204
Iglesias-Páramo, J., López-Martín, L., Vílchez, J. M., Petropoulou, V., & Sulentic, J. W. 2012, A&A, 539, A127
Konstantopoulos, I. S., Appleton, P. N., Guillard, P., et al. 2014, ApJ, 784, 1
Lesaffre, P., Pineau des Forêts, G., Godard, B., et al. 2013, A&A, 550, A106
Lisenfeld, U., Braine, J., Duc, P.-A., et al. 2002, A&A, 394, 823
Lisenfeld, U., Braine, J., Duc, P.-A., et al. 2004, A&A, 426, 471
Martin, T., Drissen, L., & Joncas, G. 2015, in Astronomical Data Analysis Software an Systems XXIV (ADASS XXIV), eds. A. R. Taylor, & E. Rosolowsky, ASP Conf. Ser., 495, 327
Martin, T. B., Prunet, S., & Drissen, L. 2016, MNRAS, 463, 4223
Martin, T. B., Drissen, L., & Melchior, A.-L. 2018, MNRAS, 473, 4130
McKinney, W. 2010, in Proceedings of the 9th Python in Science Conference, eds. S. van der Walt, & J. Millman, 51
Mendes de Oliveira, C., Plana, H., Amram, P., Balkowski, C., & Bolte, M. 2001, AJ, 121, 2524
Mendes de Oliveira, C., Cypriano, E. S., Sodré, Jr., L., & Balkowski, C. 2004, ApJ, 605, L17
Moles, M., Sulentic, J. W., & Márquez, I. 1997, ApJ, 485, L69
Moles, M., Marquez, I., & Sulentic, J. W. 1998, A&A, 334, 473
Ohyama, Y., Nishiura, S., Murayama, T., & Taniguchi, Y. 1998, ApJ, 492, L25
O'Sullivan, E., Giacintucci, S., Vrtilek, J. M., Raychaudhury, S., & David, L. P. 2009, ApJ, 701, 1560
Pérez, F., & Granger, B. E. 2007, Comput. Sci. Eng., 9, 21
Renaud, F., Appleton, P. N., & Xu, C. K. 2010, ApJ, 724, 80
Rodríguez-Baras, M., Rosales-Ortega, F. F., Díaz, A. I., Sánchez, S. F., & Pasquali, A. 2014, MNRAS, 442, 495
Stephan, M. 1877, MNRAS, 37, 334
Sulentic, J. W., Rosado, M., Dultzin-Hacyan, D., et al. 2001, AJ, 122, 2993
Swaters, R. A., van Albada, T. S., van der Hulst, J. M., & Sancisi, R. 2002, A&A, 390, 829
Torres-Flores, S., Mendes de Oliveira, C., de Mello, D. F., et al. 2009, A&A, 507, 723
Trancho, G., Konstantopoulos, I. S., Bastian, N., et al. 2012, ApJ, 748, 102
Trinchieri, G., Sulentic, J., Breitschwerdt, D., & Pietsch, W. 2003, A&A, 401, 173
Trinchieri, G., Sulentic, J., Pietsch, W., & Breitschwerdt, D. 2005, A&A, 444, 697
Van Der Walt, S., Colbert, S. C., & Varoquaux, G. 2011, Comput. Sci. Eng., 13, 22
Westmoquette, M. S., Smith, L. J., Gallagher, J. S., & Walter, F. 2013, MNRAS, 428, 1743
Williams, B. A., Yun, M. S., & Verdes-Montenegro, L. 2002, AJ, 123, 2417
Xu, C., Sulentic, J. W., & Tuffs, R. 1999, ApJ, 512, 178
Xu, C. K., Iglesias-Páramo, J., Burgarella, D., et al. 2005, ApJ, 619, L95

Appendix A: 15 Hα emitters in outer debris regions

A close visual inspection, guided by the HST/WFC3 images (PID 11502, PI Keith S. Noll) of the SQ outskirts of our deep SITELLE images has allowed us to define a set of 15 extra Hα regions (located in SDR, near NI, and west of SQ). In Table A.1 we show the relevant information for these Hα emitters for the regions from ID 177 to 191.

Table A.1. Positional information of 15 extra Hα emitter regions in the southern debris region, close to the NI, and to the west of SQ.

(1) Region ID	(2) α (h m s)	δ (° ′ ″)	(3) Velocity (km s^{-1})
177	22 35 58.8	+33 56 55.4	5698
178	22 35 58.1	+33 56 50.5	5695
179	22 35 57.8	+33 56 53.0	5756
180	22 35 57.8	+33 56 50.8	5590
181	22 35 57.5	+33 56 42.3	5714
182	22 35 56.7	+33 56 47.5	5748
183	22 35 57.1	+33 57 10.0	5690
184	22 35 56.7	+33 57 18.5	5714
185	22 35 54.8	+33 57 12.5	5703
186	22 35 54.5	+33 57 7.7	5754
187	22 35 54.4	+33 58 5.7	5912
188	22 35 56.0	+33 59 0.9	6401
189	22 35 56.1	+33 58 55.1	6051
190	22 35 54.6	+33 58 22.1	5867
191	22 36 1.0	+33 57 49.0	5824

Notes. The columns correspond to: (1) identifier of the Hα emission regions (ID); (2) right ascension (hours, minutes, and seconds) and declination (degrees, arcminutes, and arcseconds); (3) velocity (km s^{-1}). Information about the 15 extra Hα emitter regions is given in SDR, close to the NI, and to the west of SQ.

Appendix B: Additional table

Table B.1. Relevant information of Hα emission regions in Stephan's Quintet.

(1) Region ID	(2) α (h m s)	δ (° ′ ″)	(3) Velocity (km s^{-1})	(4) Area (kpc^2)	(5) Subzone
1$^{(\dagger)}$	22 36 20.3	+33 59 04.4	6657 ± 24	–	NGC 7320c
2	22 36 15.3	+33 59 1.9	6644 ± 3	1.0	YTT
3	22 36 15.2	+33 58 59.9	6656 ± 6	0.6	YTT
4	22 36 14.1	+33 58 1.0	6628 ± 2	1.3	YTT
5	22 36 14.0	+33 58 21.4	6664 ± 11	0.2	YTT
6	22 36 13.0	+33 57 36.5	6613 ± 5	0.5	YTT
7	22 36 12.6	+33 59 33.3	6630 ± 15	0.2	YTT
8	22 36 12.4	+33 57 30.2	6614 ± 4	1.3	YTT
9	22 36 11.8	+33 59 11.5	6648 ± 3	1.1	YTT
10	22 36 11.5	+33 58 59.6	6622 ± 1	1.3	YTT
11	22 36 11.5	+33 58 26.0	6618 ± 5	0.5	YTT
12	22 36 11.5	+33 58 30.3	6635 ± 6	0.3	YTT
13	22 36 11.4	+33 58 58.6	6612 ± 1	1.3	YTT
14	22 36 10.2	+33 57 18.5	6618 ± 2	2.3	YTT
15	22 36 10.0	+33 57 20.0	6608 ± 1	1.7	YTT
16	22 36 9.6	+33 57 17.7	6618 ± 5	0.3	YTT
17	22 36 9.4	+33 57 19.2	6598 ± 4	0.8	YTT
18	22 36 6.0	+33 58 20.0	6595 ± 7	0.3	NGC 7319 "Arm"
19	22 36 5.7	+33 57 29.9	6606 ± 5	0.5	YTT
20	22 36 4.4	+33 58 44.9	6764 ± 4	1.1	North lobe
21	22 36 4.3	+33 58 46.8	6809 ± 4	1.2	North lobe
22	22 36 4.3	+33 58 16.0	6662 ± 17	0.2	NGC 7319 "Arm"
23	22 36 4.3	+33 58 50.4	6868 ± 6	0.7	North lobe
24	22 36 4.0	+33 58 50.0	6769 ± 7	1.3	North lobe
25	22 36 3.8	+33 58 51.3	6779 ± 5	0.9	North lobe
26	22 36 3.4	+33 58 32.3	6768 ± 9	3.8	NGC 7319 Nucl.
27	22 36 3.3	+33 58 28.4	6586 ± 20	3.9	NGC 7319 Nucl.
28	22 36 3.3	+33 58 20.6	6715 ± 7	0.5	NGC 7319 "Arm"
29	22 36 3.3	+33 58 23.5	6355 ± 11	0.3	NGC 7319 Nucl.
30	22 36 3.1	+33 58 45.5	6750 ± 8	0.5	North lobe
31	22 36 3.1	+33 58 0.1	5863 ± 12	0.2	L1
32	22 36 2.9	+33 58 46.8	6799 ± 12	0.2	North lobe
33	22 36 1.4	+33 58 49.0	6049 ± 7	0.5	L2
34	22 36 1.4	+34 0 5.7	6198 ± 14	0.2	NW
35	22 36 1.0	+33 58 21.0	6381 ± 10	1.0	Bridge
36	22 36 0.9	+33 58 36.8	5988 ± 13	0.2	L2
37	22 36 0.7	+33 59 50.7	6028 ± 6	0.6	NW
38	22 36 0.6	+33 57 49.9	5849 ± 9	0.3	NI1
39	22 36 0.5	+33 58 6.3	5996 ± 7	0.6	L1
40	22 36 0.6	+33 58 17.9	6457 ± 14	0.3	Bridge
41	22 36 0.5	+33 59 2.1	6024 ± 8	0.5	L2
42	22 36 0.4	+33 57 55.3	5835 ± 4	0.7	NI1
43	22 36 0.4	+33 58 5.0	6003 ± 11	0.2	L1
44	22 36 0.4	+33 58 8.2	6057 ± 12	0.2	L1
45	22 36 0.3	+33 57 52.7	5809 ± 6	1.0	NI1
46	22 36 0.2	+33 57 57.5	5822 ± 5	0.8	NI1
47	22 36 0.2	+33 58 4.0	5913 ± 9	0.2	L1
48	22 36 0.2	+33 58 5.3	5898 ± 12	0.3	L1
49	22 36 0.2	+33 57 48.8	5797 ± 10	0.6	NI1

Notes. The columns correspond to: (1) identifier of the Hα emission regions (ID); (2) right ascension (hours, minutes, and seconds) and declination (degrees, arcminutes, and arcseconds); (3) Hα radial velocity (km s^{-1}); (4) area (kpc^2). (5) Subzone. "($\dagger$)" (ID 1) denotes the information about NGC 7320c. For regions with two velocity components we use "(a)" and "(b)" for low- and high-velocity components, respectively.

Table B.1. continued.

(1) Region ID	(2) α (h m s)	δ (° ′ ″)	(3) Velocity (km s^{-1})	(4) Area (kpc^2)	(5) Subzone
50	22 36 0.0	+33 58 4.2	5963 ± 10	0.3	L1
51[a]	22 35 60.0	+33 57 11.1	6215 ± 50	1.9	Sh1
51[b]	22 35 60.0	+33 57 11.1	6617 ± 20	1.9	Sh1
52	22 35 59.9	+33 57 51.4	5786 ± 3	1.7	NI1
53	22 36 0.0	+33 58 0.4	5907 ± 10	0.2	L1
54	22 36 0.1	+33 58 2.3	5924 ± 10	0.2	L1
55	22 36 0.0	+33 58 20.7	6093 ± 11	0.2	L1
56	22 35 60.0	+33 57 55.5	6846 ± 13	0.2	Sh3
57	22 35 60.0	+33 57 59.1	5997 ± 18	0.2	L1
58[a]	22 35 59.9	+33 57 57.5	6037 ± 14	0.6	L1
58[b]	22 35 59.9	+33 57 57.5	6325 ± 30	0.6	Sh3
59[a]	22 35 59.9	+33 58 5.2	6165 ± 16	1.6	L1
59[b]	22 35 59.9	+33 58 5.2	6621 ± 32	1.6	Sh3
60[a]	22 35 59.9	+33 58 10.0	6073 ± 14	0.3	L1
60[b]	22 35 59.9	+33 58 10.0	6612 ± 17	0.3	Sh3
61	22 35 59.9	+33 58 21.7	6046 ± 12	0.2	SSQA
62	22 35 59.9	+33 57 13.3	6438 ± 10	0.7	Sh1
63	22 35 59.8	+33 57 22.8	6265 ± 21	0.2	Sh1
64	22 35 59.8	+33 57 36.6	6616 ± 11	0.6	Sh2
65	22 35 59.7	+33 57 45.8	5787 ± 5	1.1	NI1
66[a]	22 35 59.8	+33 57 54.5	5946 ± 12	0.5	L1
66[b]	22 35 59.8	+33 57 54.5	6362 ± 14	0.5	Sh3
67	22 35 59.8	+33 57 55.5	5955 ± 13	0.5	L1
68[a]	22 35 59.7	+33 58 1.0	6025 ± 9	1.6	L1
68[b]	22 35 59.7	+33 58 1.0	6574 ± 37	1.6	Sh3
69[a]	22 35 59.8	+33 58 20.7	6081 ± 20	0.3	L1
69[b]	22 35 59.8	+33 58 20.7	6452 ± 32	0.3	Sh4
70	22 35 59.7	+33 58 25.5	6016 ± 4	0.7	SSQA
71	22 35 59.7	+33 58 27.4	6032 ± 8	0.4	SSQA
72	22 35 59.8	+33 57 18.7	6189 ± 15	0.3	Sh1
73	22 35 59.7	+33 57 13.9	6352 ± 10	0.7	Sh1
74	22 35 59.7	+33 57 35.6	6589 ± 18	0.7	Sh2
75	22 35 59.6	+33 57 38.1	5728 ± 5	1.5	NI1
76[a]	22 35 59.7	+33 58 19.7	6312 ± 27	0.6	Sh4
76[b]	22 35 59.7	+33 58 19.7	6761 ± 35	0.6	Sh4
77	22 35 59.6	+33 57 35.2	6540 ± 12	0.7	Sh2
78	22 35 59.6	+33 57 28.5	6154 ± 13	0.2	Sh1
79[a]	22 35 59.5	+33 58 5.1	6326 ± 31	1.3	Sh3
79[b]	22 35 59.5	+33 58 5.1	6823 ± 10	1.3	Sh3
80[a]	22 35 59.6	+33 58 17.4	6343 ± 19	0.3	Sh4
80[b]	22 35 59.6	+33 58 17.4	6752 ± 23	0.3	Sh4
81[a]	22 35 59.5	+33 58 30.3	6123 ± 17	0.3	L1
81[b]	22 35 59.5	+33 58 30.3	6734 ± 26	0.3	Sh4
82	22 35 59.5	+33 59 39.6	6017 ± 4	1.0	NW
83[a]	22 35 59.4	+33 57 33.3	6211 ± 22	3.0	Sh2
83[b]	22 35 59.4	+33 57 33.3	6626 ± 11	3.0	Sh2
84	22 35 59.5	+33 57 50.6	6767 ± 12	0.3	Sh3
85	22 35 59.5	+33 57 55.4	6735 ± 10	0.3	Sh3
86[a]	22 35 59.4	+33 58 7.0	6059 ± 13	0.8	L1
86[b]	22 35 59.4	+33 58 7.0	6350 ± 25	0.8	Sh3
87[a]	22 35 59.5	+33 58 11.5	6299 ± 21	0.3	Sh3
87[b]	22 35 59.5	+33 58 11.5	6863 ± 16	0.3	Sh3
88	22 35 59.5	+33 58 13.8	6168 ± 18	0.2	L1
89[a]	22 35 59.5	+33 58 26.4	6542 ± 22	0.7	Sh4
89[b]	22 35 59.5	+33 58 26.4	6861 ± 36	0.7	Sh4
90	22 35 59.4	+33 58 29.9	6022 ± 5	0.8	SSQA
91	22 35 59.4	+33 58 31.3	6026 ± 10	0.4	SSQA
92	22 35 59.5	+33 58 34.2	5999 ± 7	0.5	SSQA
93	22 35 59.4	+33 57 25.3	6148 ± 11	0.2	Sh1

Table B.1. continued.

(1) Region ID	(2) α (h m s)	δ (° ′ ″)	(3) Velocity (km s^{-1})	(4) Area (kpc^2)	(5) Subzone
94[a]	22 35 59.5	+33 57 35.9	5749 ± 15	0.3	NI1
94[b]	22 35 59.5	+33 57 35.9	6049 ± 28	0.3	Sh2
95[a]	22 35 59.4	+33 57 42.9	6091 ± 57	0.3	Sh2
95[b]	22 35 59.4	+33 57 42.9	6442 ± 27	0.3	Sh2
96	22 35 59.3	+33 58 24.4	6803 ± 11	0.8	H2
97	22 35 59.2	+33 59 34.6	5986 ± 5	0.6	NW
98	22 35 59.3	+33 58 27.0	6031 ± 7	0.4	SSQA
99	22 35 59.4	+33 57 27.5	6166 ± 23	0.2	Sh1
100[a]	22 35 59.4	+33 57 41.0	6233 ± 27	0.3	Sh3
100[b]	22 35 59.4	+33 57 41.0	6490 ± 34	0.3	Sh2
101	22 35 59.4	+33 57 53.2	6692 ± 16	0.2	Sh3
102[a]	22 35 59.3	+33 58 1.2	6267 ± 17	0.3	Sh3
102[b]	22 35 59.3	+33 58 1.2	6644 ± 43	0.3	Sh3
103[a]	22 35 59.3	+33 58 5.7	6030 ± 13	0.5	L1
103[b]	22 35 59.3	+33 58 5.7	6316 ± 42	0.5	Sh3
104[a]	22 35 59.4	+33 58 13.4	6124 ± 72	1.6	Sh4
104[b]	22 35 59.4	+33 58 13.4	6460 ± 31	1.6	Sh4
105	22 35 59.2	+33 58 25.7	6911 ± 11	0.6	H2
106	22 35 59.2	+33 58 32.2	6021 ± 8	0.7	SSQA
107	22 35 59.2	+33 57 53.1	6707 ± 13	0.8	Sh3
108	22 35 59.2	+33 58 0.2	6558 ± 27	0.2	Sh3
109	22 35 59.2	+33 58 16.3	6532 ± 19	0.2	Sh4
110	22 35 59.2	+33 58 22.1	6817 ± 8	0.8	H2
111	22 35 59.2	+33 58 46.8	7000 ± 6	0.5	H1
112	22 35 59.1	+33 59 4.3	6032 ± 4	1.9	L2
113	22 35 59.1	+33 57 49.9	6768 ± 9	0.3	Sh3
114	22 35 59.1	+33 58 3.1	6427 ± 14	0.3	Sh3
115	22 35 59.1	+33 58 21.1	6797 ± 13	0.4	H2
116	22 35 59.1	+33 58 25.4	6885 ± 8	1.4	H2
117	22 35 59.0	+33 57 33.2	5675 ± 1	2.2	NI1
118	22 35 59.1	+33 58 1.1	5827 ± 9	0.3	NI1
119	22 35 59.1	+33 58 5.0	6469 ± 18	0.2	Sh3
120	22 35 59.0	+33 58 34.1	6031 ± 3	1.5	SSQA
121	22 35 59.0	+33 58 45.7	6672 ± 4	3.0	SQA
122	22 35 58.8	+33 58 48.6	6680 ± 2	4.9	SQA
123	22 35 58.9	+33 58 58.1	6818 ± 10	0.2	H1
124	22 35 58.8	+33 59 35.5	6032 ± 9	0.3	NW
125	22 35 58.8	+33 57 36.0	5799 ± 11	0.7	NI2
126	22 35 58.6	+33 58 56.0	6881 ± 8	1.1	H1
127	22 35 58.8	+33 57 33.2	5744 ± 4	1.4	NI2
128	22 35 58.7	+33 57 34.1	5708 ± 3	0.7	NI2
129	22 35 58.4	+33 58 51.1	6017 ± 2	2.3	NSQA
130	22 35 58.6	+33 57 47.5	5703 ± 3	1.1	NI3
131	22 35 58.6	+33 58 54.4	6856 ± 11	0.6	H1
132	22 35 58.4	+33 58 52.4	6009 ± 2	1.4	NSQA
133	22 35 58.4	+33 57 32.8	5643 ± 1	1.8	NI2
134	22 35 58.4	+33 57 42.4	5624 ± 5	1.0	NI3
135	22 35 58.4	+33 58 48.5	6001 ± 6	1.2	NSQA
136	22 35 58.1	+33 58 54.3	6013 ± 3	1.8	NSQA
137	22 35 58.1	+33 58 46.5	6001 ± 3	2.1	NSQA
138	22 35 58.2	+33 57 29.9	5630 ± 2	1.6	NI2
139	22 35 58.0	+33 58 59.1	5987 ± 2	1.6	NSQA
140	22 35 57.9	+33 58 50.3	5987 ± 5	1.4	NSQA
141	22 35 57.8	+33 58 56.5	5984 ± 2	1.8	NSQA
142	22 35 57.8	+33 58 54.2	5983 ± 3	1.5	NSQA
143	22 35 57.6	+33 58 45.1	5980 ± 3	2.4	NSQA
144	22 35 58.0	+33 57 8.8	5650 ± 13	0.2	SDR
145	22 35 57.7	+33 59 9.8	5994 ± 11	0.2	NSQA
146	22 35 57.5	+33 58 59.6	5981 ± 2	2.2	NSQA

Table B.1. continued.

(1) Region ID	(2) α (h m s)	δ (° ′ ″)	(3) Velocity (km s^{-1})	(4) Area (kpc^2)	(5) Subzone
147	22 35 57.4	+33 58 45.3	5974 ± 8	0.3	NSQA
148	22 35 57.4	+33 58 36.6	5994 ± 5	0.6	L4
149	22 35 57.4	+33 57 34.8	5613 ± 7	0.5	NI4
150	22 35 57.0	+33 57 34.8	5615 ± 6	0.4	NI4
151	22 35 57.0	+33 57 35.7	5626 ± 7	0.4	NI4
152	22 35 56.8	+33 57 36.6	5653 ± 5	0.7	NI4
153	22 35 56.6	+33 57 37.6	5684 ± 3	1.4	NI4
154	22 35 56.5	+33 58 17.0	5955 ± 3	1.2	L4
155	22 35 56.4	+33 58 19.9	5911 ± 4	0.7	L4
156	22 35 56.3	+33 57 6.7	5674 ± 5	0.6	SDR
157	22 35 56.3	+33 57 42.9	5717 ± 4	1.0	NI4
158	22 35 56.3	+33 57 19.4	5699 ± 8	0.2	SDR
159	22 35 56.2	+33 57 44.2	5727 ± 5	1.4	NI4
160	22 35 56.1	+33 57 7.0	5695 ± 6	0.3	SDR
161[a]	22 35 55.9	+33 59 7.4	6108 ± 26	1.9	L3
161[b]	22 35 55.9	+33 59 7.4	6473 ± 68	1.9	L3
162	22 35 56.0	+33 59 11.0	6064 ± 9	0.3	L3
163	22 35 56.1	+33 56 53.1	5625 ± 10	0.2	SDR
164	22 35 55.6	+33 57 37.4	5768 ± 1	2.8	NI5
165	22 35 55.5	+33 57 43.1	5776 ± 1	2.5	NI5
166	22 35 55.4	+33 57 44.7	5790 ± 2	1.4	NI5
167	22 35 55.3	+33 57 33.5	5751 ± 2	1.7	NI5
168	22 35 55.3	+33 57 10.3	5722 ± 2	1.1	SDR
169	22 35 55.2	+33 57 11.6	5750 ± 3	0.7	SDR
170	22 35 54.9	+33 57 9.7	5705 ± 3	1.0	SDR
171	22 35 54.3	+33 57 15.9	5768 ± 3	1.3	SDR
172	22 35 54.2	+33 57 29.5	5873 ± 2	1.1	SDR
173	22 35 54.2	+33 57 15.3	5786 ± 2	1.0	SDR
174	22 35 54.1	+33 57 16.2	5793 ± 2	1.4	SDR
175	22 35 53.9	+33 57 14.3	5797 ± 5	0.7	SDR
176	22 35 49.9	+33 56 36.5	6247 ± 6	1.4	NG